

# Superior Lithium Storage Capacity of $\alpha$ -MnS Nanoparticles Embedded in S-Doped Carbonaceous Mesoporous Frameworks

Yuan Ma, Yanjiao Ma, Guk-Tae Kim, Thomas Diemant, Rolf-Jürgen Behm, Dorin Geiger, Ute Kaiser, Alberto Varzi,\* and Stefano Passerini\*

Herein, a Mn-based metal–organic framework is used as a precursor to obtain well-defined  $\alpha$ -MnS/S-doped C microrod composites. Ultrasmall  $\alpha$ -MnS nanoparticles (3–5 nm) uniformly embedded in S-doped carbonaceous mesoporous frameworks ( $\alpha$ -MnS/SCMFs) are obtained in a simple sulfidation reaction. As-obtained  $\alpha$ -MnS/SCMFs shows outstanding lithium storage performance, with a specific capacity of 1383 mAh g<sup>-1</sup> in the 300th cycle or 1500 mAh g<sup>-1</sup> in the 120th cycle (at 200 mA g<sup>-1</sup>) using copper or nickel foil as the current collector, respectively. The significant (pseudo)capacitive contribution and the stable composite structure of the electrodes result in impressive rate capabilities and outstanding long-term cycling stability. Importantly, in situ X-ray diffraction measurements studies on electrodes employing various metal foils/disks as current collector reveal the occurrence of the conversion reaction of CuS at (de)lithiation process when using copper foil as the current collector. This constitutes the first report of the reaction mechanism for  $\alpha$ -MnS, eventually forming metallic Mn and Li<sub>2</sub>S. In situ dilatometry measurements demonstrate that the peculiar structure of  $\alpha$ -MnS/SCMFs effectively restrains the electrode volume variation upon repeated (dis)charge processes. Finally,  $\alpha$ -MnS/SCMFs electrodes present an impressive performance when coupled in a full cell with commercial LiMn<sub>1/3</sub>Co<sub>1/3</sub>Ni<sub>1/3</sub>O<sub>2</sub> cathodes.

stability, power density, and safety.<sup>[1,3,4]</sup> Among the alternative electrode materials, transition metal sulfides (TMSs) are quite appealing due to their improved safety and high theoretical capacity (e.g., CuS: 560 mAh g<sup>-1</sup>; CoS<sub>2</sub>: 870 mAh g<sup>-1</sup>; and FeS<sub>2</sub>: 894 mAh g<sup>-1</sup>, as calculated for the full conversion reaction).<sup>[4]</sup> Important, compared to other conversion materials, e.g., oxides, TMSs usually show improved electronic conductivity as well as faster reaction kinetics due to the weaker metal–sulfur bond (compared to the metal–oxygen bond), making the conversion reaction easier.<sup>[4]</sup> In addition, the voltage hysteresis of sulfides ( $\approx 0.7$  V) is distinctly lower than that of oxides ( $\approx 0.9$  V), thus promising better energy efficiencies.<sup>[5]</sup>


Manganese sulfide ( $\alpha$ -MnS) is particularly appealing as anode material for LIBs, as it possesses a large theoretical capacity (616 mAh g<sup>-1</sup>) and a lower redox potential compared to other TMSs, such as copper, cobalt, and iron sulfides—besides being highly abundant, ecofriendly, and less expensive.<sup>[3,6,7]</sup> Despite these advantages,

the application of  $\alpha$ -MnS as anode material in LIBs has been hampered due to common problems of TMSs such as: (i) serious volume variation during repeated (dis)charge processes leading to poor cycling stability, and (ii) low rate capability arising from low electronic conductivity and Li-ion mobility.<sup>[3,7]</sup> In order to improve the lithium-ion storage performance of TMSs, many approaches have been proposed. One of the most efficient strategies, so far, is to fabricate nano/microstructured composite materials,

## 1. Introduction

Lithium-ion batteries (LIBs) have been successfully introduced in portable/mobile electronics (laptops, smart glasses, smart cells, and smart watches), and now in the new generation of electric vehicles (e.g., Tesla Motors).<sup>[1,2]</sup> However, the rapidly increasing demand for higher energy density batteries requires further breakthroughs in the electrode materials, especially in terms of cycling

Y. Ma, Y.-J. Ma, Dr. G.-T. Kim, Prof. R. J. Behm, Dr. A. Varzi, Prof. S. Passerini  
Helmholtz Institute Ulm (HIU)  
Helmholtzstrasse 11, 89081 Ulm, Germany  
E-mail: alberto.varzi@kit.edu; stefano.passerini@kit.edu

 The ORCID identification number(s) for the author(s) of this article can be found under <https://doi.org/10.1002/aenm.201902077>.

© 2019 Karlsruher Institut für Technologie. Published by WILEY-VCH Verlag GmbH & Co. KGaA, Weinheim. This is an open access article under the terms of the Creative Commons Attribution-NonCommercial-NoDerivs License, which permits use and distribution in any medium, provided the original work is properly cited, the use is non-commercial and no modifications or adaptations are made.

DOI: 10.1002/aenm.201902077

Y. Ma, Y.-J. Ma, Dr. G.-T. Kim, Dr. A. Varzi, Prof. S. Passerini  
Karlsruhe Institute of Technology (KIT)  
P.O. Box 3640, 76021 Karlsruhe, Germany  
Dr. T. Diemant, Prof. R. J. Behm  
Institute of Surface Chemistry and Catalysis  
Ulm University  
Albert-Einstein-Allee 47, 89081 Ulm, Germany  
Dr. D. Geiger, Prof. U. Kaiser  
Central Facility for Electron Microscopy  
Group of Electron Microscopy of Materials Science  
Ulm University  
Albert-Einstein-Allee 11, 89081 Ulm, Germany

consisting of nanosized TMSs particles uniformly embedded in porous carbon matrices or layers (such as carbon nanotubes (CNTs), amorphous carbon, and graphene).<sup>[3,4]</sup> This approach can effectively reduce the mechanical stress associated with the conversion reaction consequently improving the cyclability.<sup>[4,8]</sup> Additionally, the porous carbon support improves the electronic conductivity and inhibits TMSs nanoparticles from agglomeration during (dis)charge processes.<sup>[4,8]</sup> In particular, heteroatom-doped carbon matrices or layers (such as S or N-doped) could significantly improve the electrode–electrolyte wettability and provide additional Li-ion storage sites, thus further enhancing the Li-ion storage properties.<sup>[3,9,10]</sup> Nevertheless, the approaches so far reported to prepare  $\alpha$ -MnS-based composites are either complicated or costly,<sup>[8,11]</sup> thus, difficult to scale up for commercial-scale applications. Even more important, the lithium-ion storage mechanism of  $\alpha$ -MnS is not clearly understood yet,<sup>[12]</sup> which prevents the understanding and further optimization of the  $\alpha$ -MnS-based materials.

Here, the use of metal organic frameworks (MOFs), a novel class of well-defined porous and crystalline materials consisting of coordinated metal sites and organic linkers, may be helpful. Because of their high surface area, porous structure, and controllable morphology,<sup>[13–15]</sup> MOFs are particularly promising precursors and templates for the synthesis of electrochemically active materials with micro/nanostructure.<sup>[14]</sup> Under properly controlled synthesis conditions, metal or metal oxide/sulfide nanoparticles can be obtained, which are finely dispersed in a porous carbon matrix.<sup>[4,8,16]</sup> For example, Park and co-workers reported a porous ZnO/C microcomposite, obtained via a simple annealing of Zn-based MOFs in air, offering a promising lithium-ion storage performance.<sup>[16]</sup> Here, the ZnO quantum dots were encapsulated by the carbon matrix. Using Fe-based MOFs (MIL-88-Fe) as precursor, Huang et al. applied the facile sulfidation method to prepare unique C@Fe<sub>7</sub>S<sub>8</sub> nanorods which, when used as anode for LIBs, showed a stable capacity of 1148 mAh g<sup>-1</sup> for over 170 cycles.<sup>[17]</sup> In our previous work, we have successfully prepared a porous CoS<sub>2</sub>/C micropolyhedron with CNTs, using a two-step synthesis starting from zeolitic imidazolate frameworks-67. The resulting CoS<sub>2</sub> nanoparticles were uniformly embedded in the porous carbonaceous framework, presenting outstanding lithium and sodium storage properties.<sup>[4]</sup> Despite the great progresses in MOF-derived TMSs, only few reports are available regarding the synthesis of  $\alpha$ -MnS-based composites by using MOF strategies. Nonetheless, Mn-based MOFs have a great potential for the fabrication of advanced nanostructured  $\alpha$ -MnS-based composites, also including heteroatom-doped carbon layer/matrix.

In this present work we report for the first time the facile and efficient sulfidation reaction to prepare  $\alpha$ -MnS nanoparticles (3–5 nm) finely embedded in sulfur-doped carbonaceous mesoporous frameworks, employing a Mn-based MOF (with terephthalic acid as organic ligand) as the only precursor. The composite material, which is denoted as  $\alpha$ -MnS/SCMFs (S-doped carbonaceous mesoporous frameworks), is characterized by a well-defined microrod morphology. Compared with other synthesis strategies, this MOF-driven approach (i.e., a

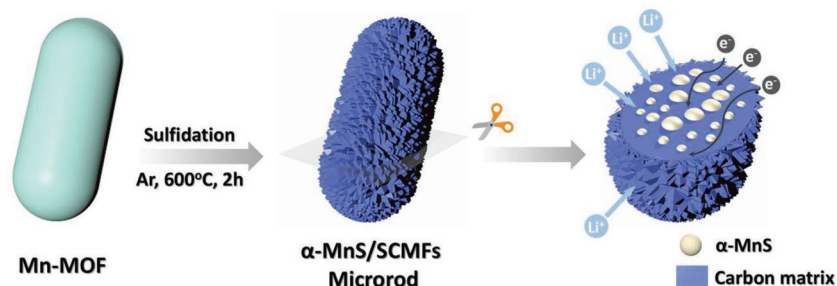
two-step synthesis) is very convenient.<sup>[3,7]</sup> The detailed physicochemical features and the electrochemical properties of this composite are reported herein. The resulting  $\alpha$ -MnS/SCMFs material features outstanding Li storage properties. More importantly, we propose a new electrochemical reaction mechanism for  $\alpha$ -MnS upon the initial (de)lithiation process, which is validated by in situ X-ray diffraction (XRD) and using different current collectors. Remarkably, the improved structural stability of the composite is further confirmed by in situ dilatometry and ex situ microscopy. Finally, the electrochemical performance of  $\alpha$ -MnS/SCMFs is evaluated in Li-ion full cells with a cathode based on commercial LiMn<sub>1/3</sub>Co<sub>1/3</sub>Ni<sub>1/3</sub>O<sub>2</sub> (NCM).

## 2. Results and Discussion

### 2.1. Synthesis and Characteristics of $\alpha$ -MnS/SCMFs

The preparation strategy of  $\alpha$ -MnS/SCMFs microrods is schematically illustrated in **Scheme 1**. Using Mn-based MOFs as the parental compound,  $\alpha$ -MnS/SCMFs microrods were obtained via the simple and mild sulfidation process described in detail in the Experimental Section. First, the Mn-based MOFs precursor was fabricated by stirring and refluxing a *N,N*-dimethylformamide (DMF)/ethanol solution containing divalent manganese nitrate and terephthalic acid at 100 °C for 12 h. The physicochemical characteristics of the precursor obtained via scanning electron microscopy (SEM), transmission electron microscopy (TEM), and powder XRD are shown in Figure S1 of the Supporting Information. As-obtained Mn-based MOFs exhibit a well-defined microrod morphology with relatively smooth surfaces (see SEM images) and a solid and dense structure, according to TEM investigation.

Afterward, the Mn-based MOF precursor was converted into  $\alpha$ -MnS/SCMFs by the sulfidation process under argon atmosphere. The Mn-MOF was first mixed with sulfur powder in a mass ratio of 1:6 and then annealed at 600 °C for 2 h. During the sulfidation, the gaseous sulfur generated at high temperature reacted with the Mn-ions in the MOF to form uniform MnS nanoparticles.<sup>[17]</sup> Meanwhile, the organic ligands were carbonized in situ and sulfurated. This resulted in a uniform carbon layer coating of the  $\alpha$ -MnS nanoparticles.<sup>[11,17]</sup> The crystal structure and phase purity of the final product were characterized by powder XRD, as shown in **Figure 1a**. All diffraction peaks could be indexed to cubic  $\alpha$ -MnS (JCPDS card



**Scheme 1.** Schematic illustration of the synthesis and lithiation process of  $\alpha$ -MnS/SCMFs. Hierarchical  $\alpha$ -MnS/SCMFs was obtained via the simple sulfidation of the Mn-MOF template in Ar. As-obtained hierarchical  $\alpha$ -MnS/SCMFs possesses advanced structural and compositional features for Li-ion storage.

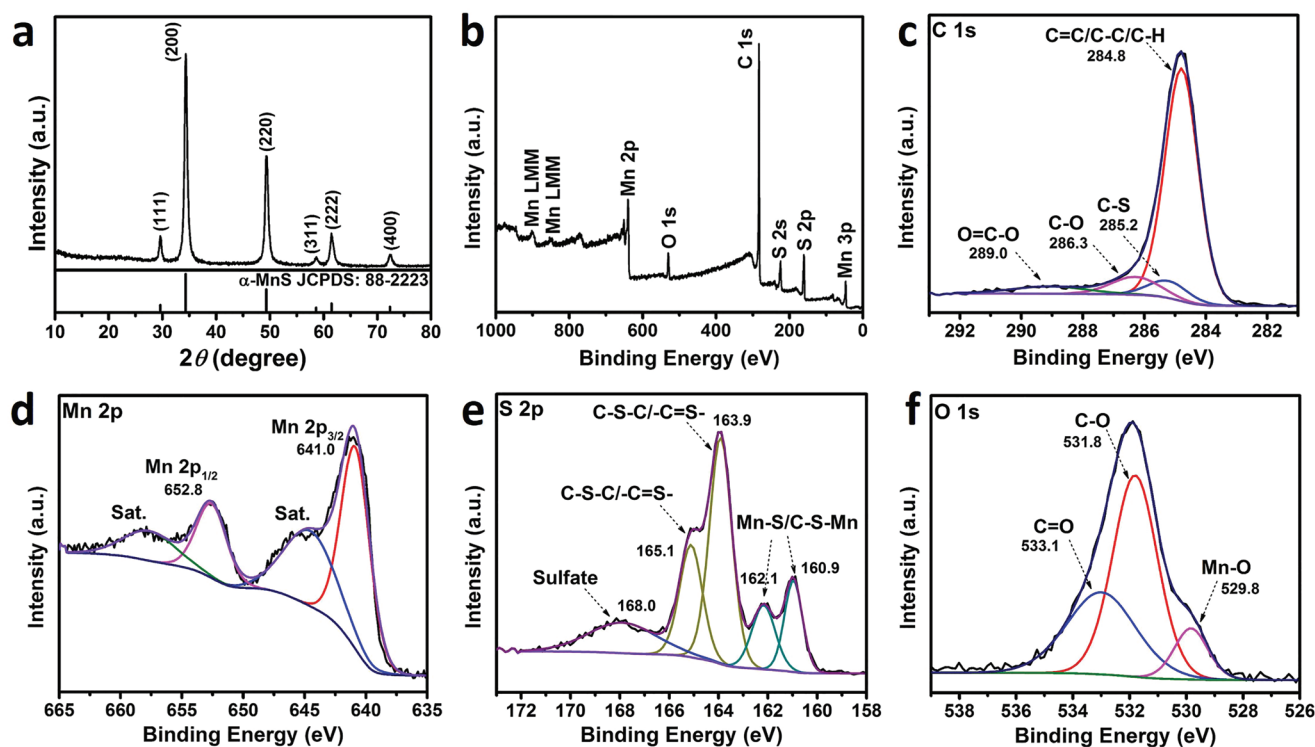


**Figure 1.** a) Powder XRD pattern of as-prepared  $\alpha$ -MnS/SCMFs, the reference for  $\alpha$ -MnS (JCPDS card No. 88-2223) is displayed in the bottom. b–f) XPS spectra of as-obtained  $\alpha$ -MnS/SCMFs: b) survey spectrum and high-resolution detail spectra of the c) C 1s, d) Mn 2p, e) S 2p, and f) O 1s regions.

No. 88-2223; space group Fm-3m). No unexpected peaks from impurities were detected. It should be noted that the Mn-MOF to S ratio can significantly affect the composition of the resulting product. In fact, as evidenced by control experiments, lower sulfur contents resulted in a MnS/MnO mixture (see XRD patterns in Figure S2 of the Supporting Information).

The surface chemistry of  $\alpha$ -MnS/SCMFs was characterized in detail by X-ray photoelectron spectroscopy (XPS). The XPS survey spectrum in Figure 1b reveals the presence of Mn, O, C, and S. Other elements were not detected, corroborating again the purity of the material. The high-resolution XPS detail spectrum of the C 1s region including the corresponding fits is displayed in Figure 1c. Four obvious peaks can be discerned at binding energies of 284.8, 285.2, 286.3, and 289.0 eV, which are attributed to C=C/C-C/C-H, C-S, C-O, and O=C-O groups, respectively, indicating the presence of sulfur and oxygen-containing groups on the surface of the porous carbonaceous framework.<sup>[9]</sup> The Mn 2p detail spectrum (Figure 1d) shows two features centered at 641.0 and 652.8 eV, which correspond to the Mn 2p<sub>3/2</sub> and Mn 2p<sub>1/2</sub> peaks.<sup>[3]</sup> The binding energies of the two peaks point to the presence of Mn<sup>2+</sup>, suggesting the presence of MnS. Additionally, two satellite peaks appear at 644.9 and 658.0 eV,<sup>[7]</sup> which are also characteristic for Mn<sup>2+</sup>. The Mn oxidation state was further tested by an analysis of the detail spectra in the range of the Mn 3s peak (Figure S3, Supporting Information). It was shown earlier that the degree of splitting of the Mn 3s peak can be used to determine the Mn oxidation state: the splitting increases from  $\approx 4.7$  eV for Mn<sup>4+</sup> to  $\approx 5.3$  eV for Mn<sup>3+</sup> and  $\approx 6$  eV for Mn<sup>2+</sup>.<sup>[18,19]</sup> For  $\alpha$ -MnS/SCMFs, the splitting is 5.9 eV, corroborating the predominance

of Mn<sup>2+</sup>. Figure 1e shows the S 2p detail spectrum, which is composed of several multiple peaks. The first doublet (S 2p<sub>3/2</sub> peak at 160.9 eV, S 2p<sub>1/2</sub> peak at 162.1 eV) can be attributed to the MnS nanoparticles. The second doublet (163.9/165.1 eV) is assigned to S atoms in the carbonaceous framework (C-S-C/-C=S-).<sup>[3,20]</sup> Finally, the broad peak located at 168.0 eV corresponds to sulfate species generated upon sample oxidation.<sup>[3,4]</sup> Taken together, the results indicate that S not only reacts with Mn atoms, but dopes the porous carbonaceous framework too.<sup>[3,4,20]</sup> Finally, the O 1s spectrum in Figure 1f displays two peaks at binding energies of 531.8 and 533.1 eV, representing the C-O and C=O groups, respectively, which is in agreement with the C 1s XPS spectrum.<sup>[7,9,21,22]</sup> It should be mentioned that there is also a small feature at 529.8 eV, suggesting the formation of MnO impurities.<sup>[9,21,22]</sup> Overall, XRD and XPS confirm that the simple and mild sulfidation of Mn-MOF successfully converted the precursor into a hybrid composite of  $\alpha$ -MnS and S-doped carbon, this latter featuring several S or O-containing functional groups. These are expected to provide extra Li-ion storage sites and, more important, improve the electrode wettability.<sup>[9,10]</sup>

SEM and TEM were used to further analyze the morphology and structure of  $\alpha$ -MnS/SCMFs. The low magnification SEM image (see Figure 2a) shows that  $\alpha$ -MnS/SCMFs possesses a uniform microrod shape with a particle size comparable to that of the Mn-MOF precursor (see Figure S1a,b of the Supporting Information), suggesting that the final product keeps the original morphology of the parental compound. The high magnification SEM images (see Figure 2b,c) reveal that, differently from the Mn-MOF precursor, the surface of the  $\alpha$ -MnS/SCMFs



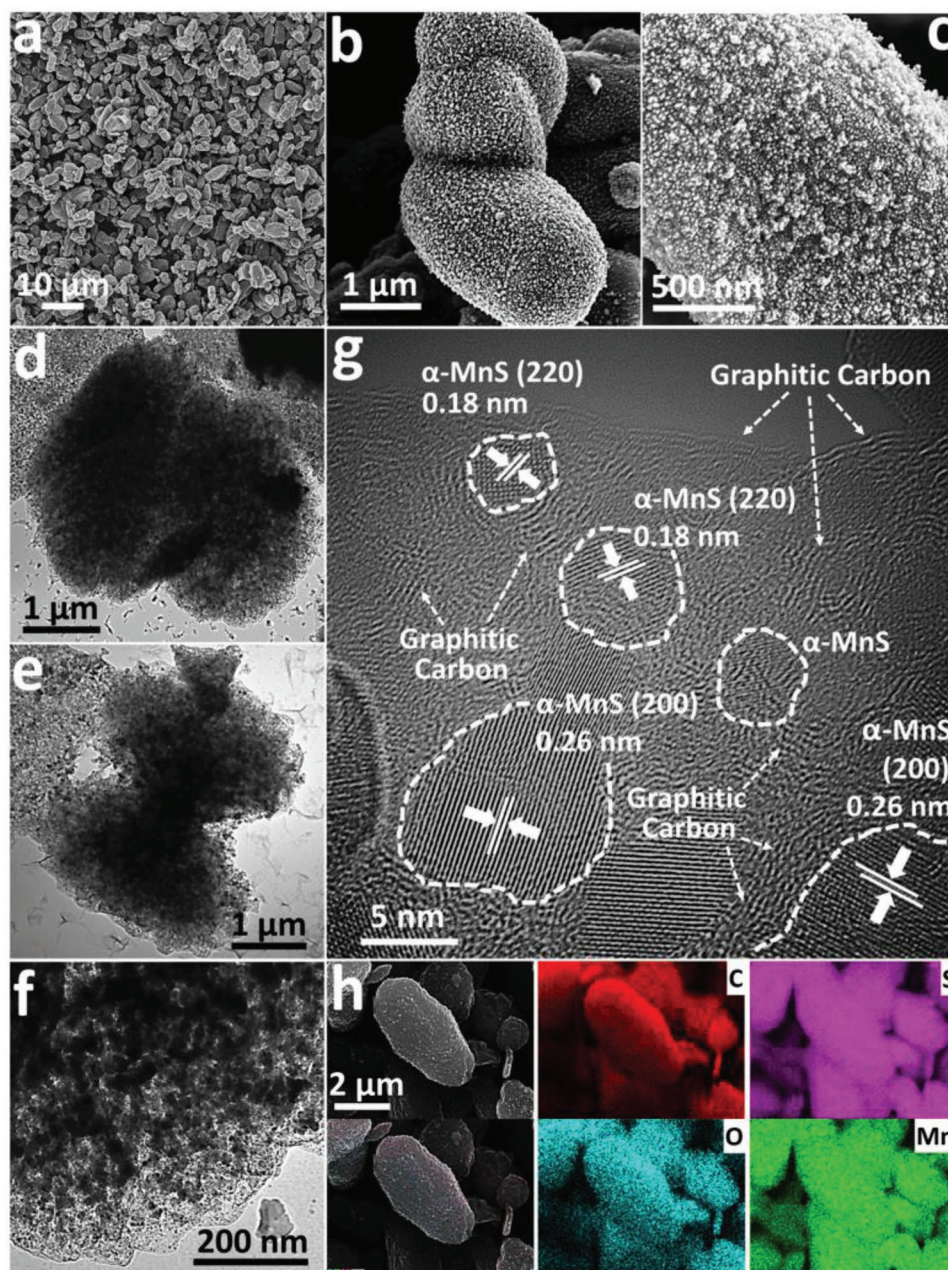


**Figure 2.** Morphological and structural characteristics of  $\alpha$ -MnS/SCMFs microrods: a–c) SEM and d–f) TEM images at different magnifications; g) HRTEM micrograph; and h) EDX elemental mapping images.

microrod particles consists of numerous nanoparticles. The TEM images in Figure 2d,e clearly demonstrate the porous nature of the  $\alpha$ -MnS/SCMFs microrods, which is caused by the release of gaseous products (like  $\text{CO}_2$ ,  $\text{H}_2\text{O}$ , and  $\text{CO}$ ) from the Mn-MOF precursor during the annealing process.<sup>[9]</sup> Furthermore, the TEM image recorded at higher magnification (Figure 2f) clearly resolves the carbon layer on the surface of the microrods. The high-resolution TEM (HRTEM) micrograph in Figure 2g and Figure S4a (Supporting Information) reveals that the  $\alpha$ -MnS nanoparticles are homogeneously embedded in the carbon matrix. As shown in Figure 2g, the lattice fringes of the  $\alpha$ -MnS nanoparticles, with  $d$ -spacings of 0.18 and 0.26 nm, can

be assigned to the (220) and (200) plane of cubic  $\alpha$ -MnS (JCPDS card No. 88-2223). Meanwhile, a layered graphitic carbon shell coats the  $\alpha$ -MnS nanoparticles. The statistical TEM analysis of the particle size, displayed in Figure S4b (Supporting Information), reveals that the large majority of the  $\alpha$ -MnS nanoparticles fall in between the 3–5 nm size. Overall, the (HR)TEM study evidences that the  $\alpha$ -MnS nanoparticles are mostly coated with a graphitic carbon layer and embedded in the porous carbonaceous microrods.<sup>[4]</sup> Finally, energy dispersive X-ray spectroscopy (EDX) elemental mapping, as shown in Figure 2h, further reveals the homogeneous co-existence and uniform distribution of C, S, O, and Mn in the  $\alpha$ -MnS/SCMFs microrods.

The Raman spectrum (see Figure S5 of the Supporting Information) of  $\alpha$ -MnS/SCMFs further confirms the co-existence of  $\alpha$ -MnS and the carbon matrix. The two peaks at 1337 and 1568  $\text{cm}^{-1}$  are attributed to the typical D and G bands of carbon, while the sharp band at 646  $\text{cm}^{-1}$  corresponds to  $\alpha$ -MnS. Based on thermogravimetric analysis (TGA) and XRD results (see Figures S6 and S7 of the Supporting Information), the weight percentage of  $\alpha$ -MnS in  $\alpha$ -MnS/SCMFs can be estimated to be around 55.1 wt%, which is only slightly larger than the value of 52.3 wt% obtained by EDX analysis (see Table S1 of the Supporting Information). This difference is probably due to the limited sampling depth of EDX. The surface area and porous structure of  $\alpha$ -MnS/SCMFs were also investigated by  $\text{N}_2$  adsorption. As shown in Figure S8a of the Supporting Information,  $\alpha$ -MnS/SCMFs presents a moderate specific Brunauer–Emmett–Teller (BET) surface area of 109  $\text{m}^2\text{g}^{-1}$ . The pore-size distribution in Figure S8b of the Supporting Information, which was evaluated based on the Barrett–Joyner–Halenda (BJH) method, evidences a pore size mainly centered at  $\approx 12$  nm, indicating a mesoporous nature of the  $\alpha$ -MnS/SCMFs. Such mesoporous character can promote electrolyte penetration and ion transport, and even buffer the volume variation during repeated (dis)charge.<sup>[4,9]</sup>

## 2.2. Detailed Lithium-Ion Storage Mechanism Study of $\alpha$ -MnS/SCMFs

Following the physicochemical characterization of the materials, the electrochemical performance of  $\alpha$ -MnS/SCMFs in the anodes of LIBs was investigated. As reference, electrodes based on pure (commercial)  $\alpha$ -MnS were also evaluated (related physicochemical characteristics are available in the Supporting Information (Figure S9 of the Supporting Information)). For the  $\alpha$ -MnS/SCMFs-based electrodes, the active material mass includes the weight of  $\alpha$ -MnS as well as that of the carbon-based component (i.e., SCMFs). First, the Li-ion storage mechanism in  $\alpha$ -MnS/SCMFs was investigated by cyclic voltammetry (CV). The results of the initial six scans of  $\alpha$ -MnS/SCMFs and  $\alpha$ -MnS-based electrodes deposited on Cu current collectors, denoted as  $\alpha$ -MnS/SCMFs/Cu and  $\alpha$ -MnS/Cu, respectively, are shown in Figure 3a–c. The first cycle for  $\alpha$ -MnS/SCMFs/Cu displays characteristics similar to  $\alpha$ -MnS/Cu (see Figure 3a). In the voltage range between 1.5 and 0.01 V, two redox peaks, located at 0.52 V in the cathodic sweep and 1.30 V in the anodic sweep, are observed for both  $\alpha$ -MnS/SCMFs/Cu and  $\alpha$ -MnS/Cu. They are assigned to the conversion of manganese sulfide with  $\text{Li}^+$  ions (i.e., reduction and oxidation of Mn for the cathodic and anodic peaks) and to the decomposition of the electrolyte to form the solid electrolyte interphase (SEI) layer (only the cathodic peak).<sup>[3,7]</sup> Furthermore, compared to  $\alpha$ -MnS/Cu,  $\alpha$ -MnS/SCMFs/Cu shows an additional distinct cathodic feature below 0.1 V, which is attributed to the insertion/intercalation of  $\text{Li}^+$  ions into the carbonaceous framework of  $\alpha$ -MnS/SCMFs.<sup>[4]</sup> Interestingly, the CV curve of  $\alpha$ -MnS/SCMFs/Cu shows, in the voltage range 3.0–1.5 V, two small cathodic peaks centered at 2.03 and 1.69 V, and three features in the initial anodic sweep at 1.89, 2.36, and 2.70 V, respectively. The cathodic peak at 1.69 V and two anodic peaks at 1.89 and

2.36 V appear also in the initial CV of  $\alpha$ -MnS/Cu (see Figure S10 of the Supporting Information). As previously reported, the cathodic peak at about 1.69 V can be explained by lithium insertion into  $\alpha$ -MnS to generate the intermediate  $\text{Li}_3\text{MnS}$ , and the anodic peaks at 1.89 and 2.36 V can be assigned to the de-insertion of Li ions from the MnS lattice or defects in the composite.<sup>[3,12,23–25]</sup> Furthermore, it was reported that the broad feature at 2.70 V in the anodic sweep could be due to the further oxidation of  $\text{Mn}^{2+}$  to obtain  $\text{MnS}_{1+z}$  ( $0 < z \leq 1$ ).<sup>[20]</sup> However, as it will be shown later, the real origin of these features is a side reaction involving the Cu current collector. Overall,  $\alpha$ -MnS/SCMFs/Cu exhibited a higher specific current than  $\alpha$ -MnS/Cu, which can be explained by a (pseudo)capacitive contribution (to be discussed later in more detail)<sup>[26]</sup> and additional lithium-ion storage sites provided by the S-doped carbon matrix.

In the following sweeps (second to sixth cycles), two new cathodic peaks evolve at  $\approx 0.60$  and 0.35 V on  $\alpha$ -MnS/SCMFs/Cu (see Figure 3b), which are quite different from the initial reduction peak located at 0.52 V. This difference is ascribed to some irreversible processes in the initial scan, such as the formation of the SEI layer and the structural rearrangement of  $\alpha$ -MnS caused by lithium-ion activation (to be discussed later in more detail).<sup>[7]</sup> Nevertheless, differently from  $\alpha$ -MnS/Cu (in Figure 3c), the voltammograms of  $\alpha$ -MnS/SCMFs/Cu largely overlap from the second cycle onward, underlining the excellent reversibility of  $\alpha$ -MnS/SCMFs upon repeated (de)lithiation cycles.<sup>[4,9,27]</sup>

To understand the electrochemical behavior of  $\alpha$ -MnS/SCMFs/Cu in LIBs, especially with regard to the (pseudo)capacitive-controlled contribution, a kinetic analysis was performed by CV measurements at different scan rates, i.e., from 0.05 to 2.0  $\text{mV s}^{-1}$ . CV curves of  $\alpha$ -MnS/SCMFs/Cu for the various scan rates are exhibited in Figure 3d and Figure S11 (Supporting Information). Noticeably, the shape of the curves is well preserved when increasing the sweep rate from 0.1 to 1.0  $\text{mV s}^{-1}$  (see Figure 3d), suggesting minor polarization at these rates. As previously reported, the contribution from capacitive effects at a fixed potential can be characterized by determining the relationship between the recorded current ( $I$ ) and the sweep rate ( $\nu$ ) using the following equation:  $I = a\nu^b$ , where both  $a$  and  $b$  are adjustable parameters.<sup>[4,26]</sup> The  $b$ -value, which can be determined by plotting  $\log I$  versus  $\log \nu$ , can reveal different electrochemical behaviors at a given potential. In general, a  $b$ -value of 0.5 suggests for a completely diffusion-controlled process (e.g., insertion/conversion/alloying reaction), whereas  $b = 1$  indicates the ideal, surface-limited capacitive behavior.<sup>[26,28]</sup> Figure 3e shows the calculated anodic  $b$ -values for  $\alpha$ -MnS/SCMFs/Cu and  $\alpha$ -MnS/Cu, which are determined for the anodic current peak at 1.30 V. Compared to the  $b$ -value of 0.51 for  $\alpha$ -MnS/Cu, the value calculated for the anodic peak of  $\alpha$ -MnS/SCMFs/Cu (0.81) indicates a higher capacitive contribution in  $\alpha$ -MnS/SCMFs/Cu.<sup>[29]</sup>

By separating the current response  $i$  at a given voltage into the capacitive ( $k_1\nu$ ) and diffusion-dominated process ( $k_2\nu^{1/2}$ ), the (pseudo)capacitive contribution can be quantitatively determined according to the following relation:  $i(V) = k_1\nu + k_2\nu^{1/2}$ , where  $k_1$  and  $k_2$  are constants, and  $i(V)$  is the measured total current response at a fixed potential  $V$ .<sup>[26,29]</sup> By plotting  $i(V)/\nu^{1/2}$  versus  $\nu^{1/2}$ , the  $k_1$ -value at a particular potential can be obtained from the



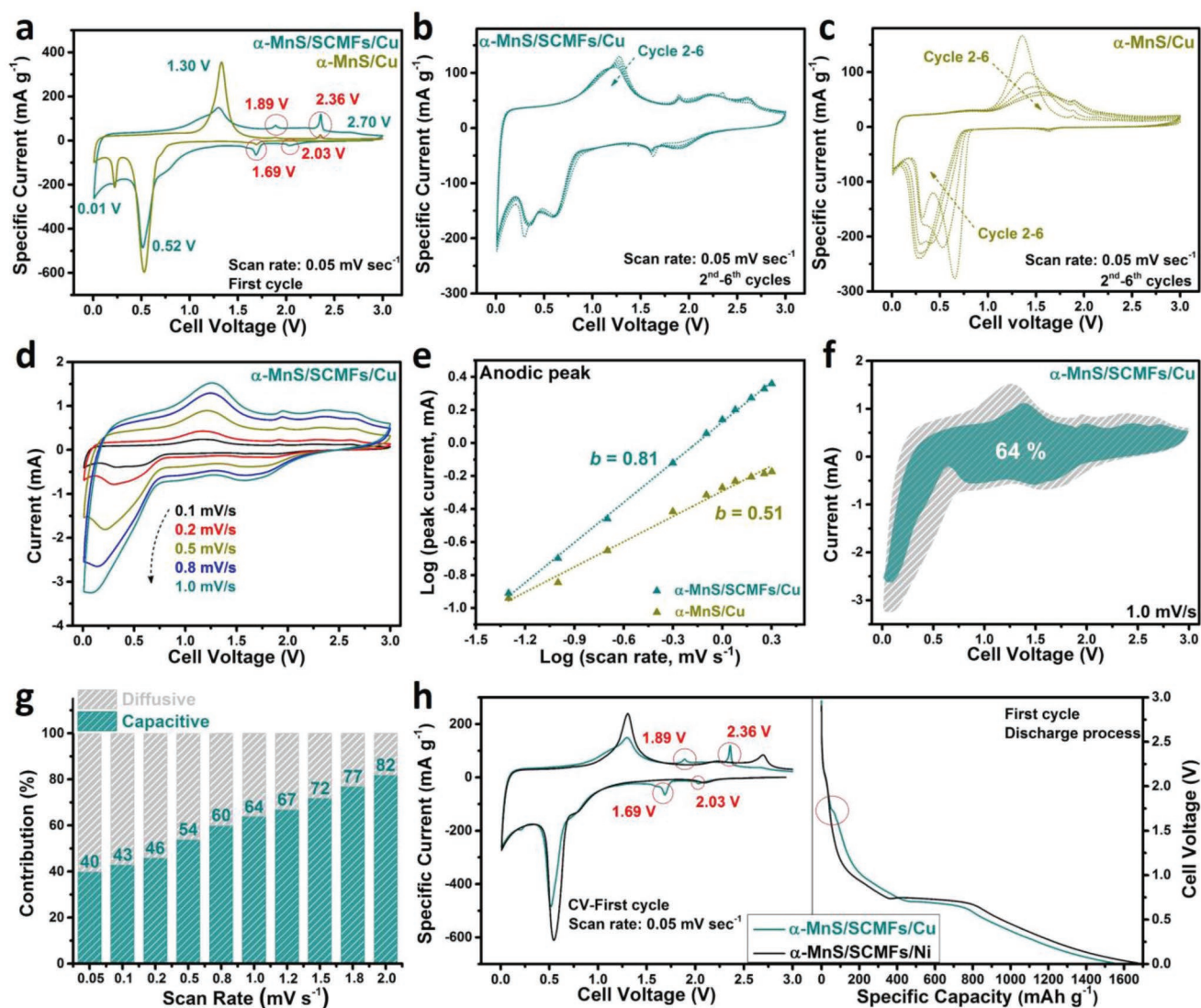


**Figure 3.** Cyclic voltammetry curves of  $\alpha$ -MnS/SCMFs/Cu and  $\alpha$ -MnS/Cu during a) the first cycle and b,c) second to sixth cycles, recorded at the sweep rate of  $0.05 \text{ mV s}^{-1}$  in the potential range of  $0.01$ – $3.0 \text{ V}$ . Kinetic analysis of the lithium storage behavior: d) CV profiles of  $\alpha$ -MnS/SCMFs/Cu at various scan rates; e) calculated  $b$ -value of  $\alpha$ -MnS/SCMFs/Cu and  $\alpha$ -MnS/Cu via plotting the logarithmic anodic peak current versus the logarithm scan rate; f) (pseudo)capacitive (cyan area) and diffusive-controlled (grey area) contributions to the overall lithium storage in  $\alpha$ -MnS/SCMFs/Cu at a scan rate of  $1.0 \text{ mV s}^{-1}$ ; g) normalized contribution ratio of (pseudo)capacitive (cyan area) and diffusion-controlled (grey area) charge storage in the  $\alpha$ -MnS/SCMFs/Cu at various scan rates, from  $0.05$  to  $2.0 \text{ mV s}^{-1}$  (see Figure S11 in the Supporting Information for the corresponding CV profiles). h) Comparison between  $\alpha$ -MnS/SCMFs/Cu and  $\alpha$ -MnS/SCMFs/Ni: the CV curves for the initial cycle (left panel) with a sweep rate of  $0.05 \text{ mV s}^{-1}$  in a potential range of  $0.01$ – $3.0 \text{ V}$  and the voltage profile of the initial lithiation (discharge) process (right panel) when applying a constant specific current of  $50 \text{ mA g}^{-1}$ .

slope, while the intercept is the  $k_2$ -value. This way, the percentage of the contribution from capacitive and diffusion-controlled processes can be determined for  $\alpha$ -MnS/SCMFs/Cu. Figure 3f shows the results of this analysis for a sweep rate of  $1.0 \text{ mV s}^{-1}$ . At this sweep rate,  $\approx 64\%$  of the total charge results from (pseudo)capacitive processes (highlighted by the cyan shaded area). As expected, the capacitive contribution gradually increases with the sweep rate from  $0.05$  to  $2.0 \text{ mV s}^{-1}$ , as shown in Figure 3g. At the maximum scan rate of  $2.0 \text{ mV s}^{-1}$ , the value of the capacitive contribution ratio has increased to  $82\%$ . This trend is attributed to the mesoporous structure and the large surface area of  $\alpha$ -MnS/SCMFs, suggesting this material has very good rate capability.

Next, the electrochemical reaction mechanism of  $\alpha$ -MnS/SCMFs was further investigated using different current collectors. Generally, according to previously reported studies,  $\alpha$ -MnS undergoes a successive two-step lithiation process by insertion ( $\approx 1.59$ – $1.69 \text{ V}$ ) and conversion ( $\approx 0.4$ – $0.5 \text{ V}$ ).<sup>[3,12,23–25,30,31]</sup> Interestingly, when the slurry of  $\alpha$ -MnS/SCMFs is coated on a nickel foil ( $\alpha$ -MnS/SCMFs/Ni), the first CV curve of the resulting electrodes in the voltage range from  $1.0$  to  $3.0 \text{ V}$  reveals a different electrochemical behavior compared to  $\alpha$ -MnS/SCMFs/Cu (see Figure 3h (left panel) and Figure S12 of the Supporting Information). The two cathodic peaks at  $2.03$  and  $1.69 \text{ V}$  and the anodic features at  $1.89$  and  $2.36 \text{ V}$  do not appear in the

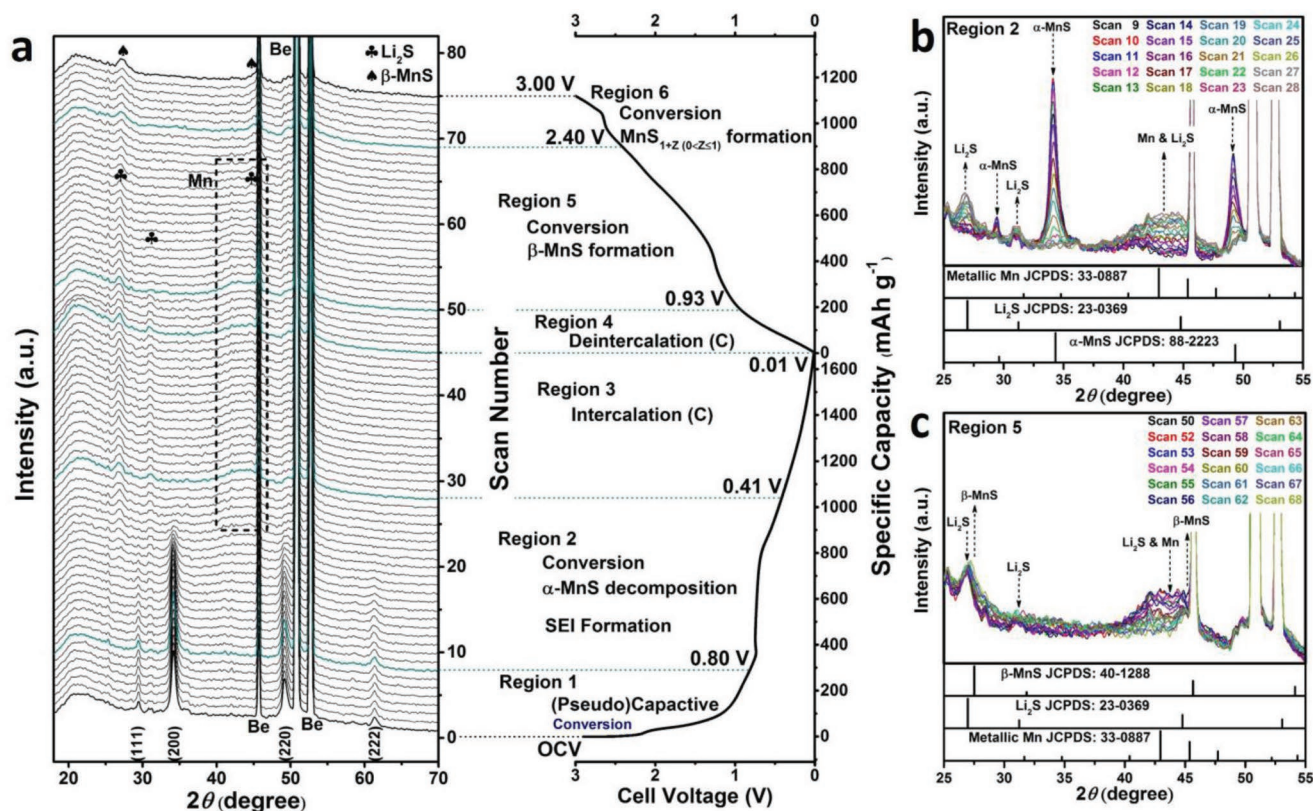


**Figure 4.** In situ XRD characterization of the  $\alpha$ -MnS/SCMFs electrode in a two-electrode cell during galvanostatic (dis)charge versus lithium metal, using a beryllium (Be) disk as current collector. a) Waterfall diagram of the sequentially collected diffractograms (scans 1–75; left panel) and the corresponding first lithiation/delithiation profile (right panel). Details on the evolution of the diffractograms in selected  $2\theta$  regions: b) region 2, scans 9–28; c) region 5, scans 50–68. Other regions are displayed in Figure S13, S16, and S17 of the Supporting Information.

initial voltammetric scan of  $\alpha$ -MnS/SCMFs/Ni. Similarly, the discharge profile of  $\alpha$ -MnS/SCMFs/Ni displays no plateau at 1.70 V (see Figure 3h, right panel), which would correspond to the CV peak at 1.69 V.<sup>[24,25,30,31]</sup>

To explain the differences observed for the electrodes coated on Cu or Ni current collector, and to gain a deeper understanding of the reaction mechanism, in situ XRD measurements were performed during the initial discharge (from open-circuit voltage (OCV) to 0.01 V) and charge (from 0.01 to 3.0 V) by means of an in-house-designed, in situ cell (two-electrode system) with a beryllium (Be) disk as current collector for the working electrode and Li metal as counter electrode.<sup>[4,9,27,32]</sup> Figure 4a displays all recorded diffractograms (75 scans, left panel), and the corresponding voltage profile (right panel). Based on the dynamic phase change evident from the diffractograms, in analogy with the CV results (Figure 3h, left part), which are highlighted by the cyan scans in the waterfall XRD panel.

In region 1, from OCV to 0.80 V (lithiation), the XRD patterns (scans 1 to 8; Figure 4a, left part) do not show an obvious phase variation of  $\alpha$ -MnS, as evidenced by the almost complete match between scan 1 (OCV) and scan 8 (0.80 V; see Figure S13 of the Supporting Information). Similar to  $\alpha$ -MnS/SCMFs/Ni, the plateau feature at  $\approx 1.7$  V is absent in the discharge profile of the in situ cell (Figure 4a, right panel), which in fact does not employ Cu as current collector. Based on these data and

the kinetic analysis (see Figure S14 of the Supporting Information), the charge storage in region 1 clearly does not originate from Li insertion into the  $\alpha$ -MnS crystal to form  $\text{Li}_x\text{MnS}$ , but mainly results from (pseudo)capacitive contributions (possibly including a small contribution from the reduction process of  $\text{Mn}^{3+}$  ( $2 < x \leq 4$ )). Importantly, we have carefully analyzed the available literature on  $\alpha$ -MnS as anode material in LIBs. It was found that the CV-redox peak couples (cathodic peaks at 2.03 and 1.69 V, anodic peaks at 1.89 and 2.36 V) and the corresponding plateaus in the voltage profile appeared only when  $\alpha$ -MnS-based slurries were coated on Cu foil.<sup>[3,7,12,23–25,30,31,33]</sup> For other types of  $\alpha$ -MnS-based electrode materials, like nickel foam as current collector or self-supported  $\alpha$ -MnS@carbon nanofibers,<sup>[20,34,35]</sup> such features were absent. Thus, we believe that these features are instead related to a two-step conversion process (reduction/oxidation) of CuS, which matches well with the previously reported study on CuS as LIBs electrode material by Yuan et al.<sup>[36]</sup> It is reasonable to believe that CuS possibly results from the sulfidation of Cu foil in contact with MnS and/or residual elemental S in the samples. The CV profiles of the current collectors (Ni and Cu foils; see Figure S15 of the Supporting Information) recorded after the removal of the electrode coating layer further confirm our conclusion.

In the second discharge region, occurring in the voltage range from 0.80 to 0.41 V, the main, long plateau is observed (Figure 4a, right panel), which corresponds to the cathodic peak



at around 0.52 and 0.56 V in the first CV of  $\alpha$ -MnS/SCMFs/Cu and  $\alpha$ -MnS/SCMFs/Ni, respectively (see Figure 3h). The related diffractograms (scans 9 to 28), which are collected in Figure 4b, (i.e., region 2), show a pronounced decrease in intensity of the  $\alpha$ -MnS (111), (200) and (220) planes, until their full disappearance at scans 24–25, which do not obviously shift to lower  $2\theta$  values. At the same time, two new features gradually evolve at  $26.8^\circ$  and  $31.1^\circ$ , suggesting the formation of  $\text{Li}_2\text{S}$  (JCPDS card no. 23–0369). Also, a new broad reflection in the  $39\text{--}48^\circ$  range grows continuously, which includes the reflections of metallic Mn (JCPDS card No. 33-0887) and of the  $\text{Li}_2\text{S}$  (220) plane. Important, after the scans 24/25 (i.e., the complete disappearance of the  $\alpha$ -MnS reflections) the intensity of this broad feature gradually increases until scan 28, suggesting that the conversion of  $\alpha$ -MnS to metallic Mn and  $\text{Li}_2\text{S}$  is completed at about 0.4 V. Furthermore, compared to the second to sixth CV cycles of  $\alpha$ -MnS/SCMFs/Cu (see Figure 3b), the first CV sweep also demonstrates that the SEI layer formation provides a partial contribution to the discharge capacity in region 2.

Upon complete lithiation to 0.01 V (region 3) the voltage profile shows a less steep slope, corresponding to the last cathodic feature recorded in the CV curve at around 0.01 V. Due to the very small crystalline domains, the dynamic variation of the diffractograms (scans 29–45) associated to the insertion/intercalation of Li-ions into graphitic carbon to obtain  $\text{Li}_y\text{C}_6$ , which is known to proceed within this voltage range, is not observed in Figure 4a (left panel).<sup>[4,37]</sup> Similarly, for the subsequent charge process (delithiation, region 4), although the charge capacity in region 4 (corresponding to the range 0.01–0.93 V; see Figure 4a, right panel) mainly stems from the Li de-insertion/de-intercalation process from  $\text{Li}_y\text{C}_6$ , no obvious changes can be observed in the related diffractograms (scans 45–50).<sup>[4,37]</sup>

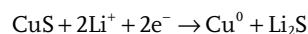
Upon further charge to 2.40 V, i.e., in region 5 (delithiation, from 0.93 to 2.40 V), the voltage profile shows a distinct plateau at about 1.30 V, followed by a slope that corresponds to the anodic peak at around 1.30 V in the CV sweeps of both  $\alpha$ -MnS/SCMFs/Cu and  $\alpha$ -MnS/SCMFs/Ni. The corresponding XRD patterns (scans 50–68; Figure 4c) reveal a sharp intensity decline of all  $\text{Li}_2\text{S}$  and  $\text{Mn}^0$ -related features until their complete disappearance in scans 65/66. Despite the very low intensity, two new reflections seem to gradually evolve at  $27.2^\circ$  and  $45.5^\circ$ , matching well with the (111) and (220) planes of  $\beta$ -MnS (JCPDS card No. 40-1288). This suggests that the re-conversion process of metallic Mn to MnS occurs in region 5 (the phase change in this region is more obvious from the direct comparison of the three scans 50, 59, and 68; Figure S16, Supporting Information). Based on the behavior observed in region 5,  $\alpha$ -MnS appears to undergo a substantial structural rearrangement at the end of the first cycle, finally resulting in the  $\beta$ -MnS phase. Our findings are in good agreement with the ex situ XRD results reported by Liu et al.<sup>[7]</sup>

Finally, in region 6 (from 2.40 to 3.00 V), the charge profile shows a small plateau located at 2.64 V, corresponding to the anodic CV peak at 2.7 V of both  $\alpha$ -MnS/SCMFs/Cu and  $\alpha$ -MnS/SCMFs/Ni. However, no obvious change in the diffractograms can be observed in this region (see the left panel of Figure 4a and Figure S17 of the Supporting Information). As previously observed by ex situ TEM and XPS measurements for  $\text{Mn}_2\text{O}_3$  as anode in LIBs, only  $\text{Mn}_3\text{O}_4$  can be detected when

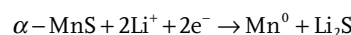
the electrode is charged to 2.0 V, while the higher oxidation states of manganese ( $\text{Mn}^{3+}/\text{Mn}^{4+}$ ) can be accessed when fully charging to the cutoff potential of 3.0 V.<sup>[20,38]</sup> Analogously, the small feature observed in our case could be attributed to the partial oxidation of  $\text{Mn}^{2+}$  to a higher oxidation state, therefore suggesting the formation of  $\text{MnS}_{1+z}$  ( $0 < z \leq 1$ ).

In summary, according to the above-discussed findings, the first-cycle reaction mechanism of  $\alpha$ -MnS/SCMFs may be described as follows:

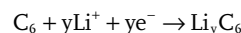
**Region 1** (OCV– 0.80 V, CuS conversion only with Cu foil as current collector)



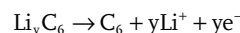
**Region 2** (0.80 – 0.41 V, MnS conversion)



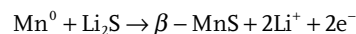
**Region 3** (0.41 – 0.01 V, Li insertion/intercalation in graphitic carbon)



**Region 4** (0.01 – 0.93 V, Li de-insertion/de-intercalation from graphitic carbon)



**Region 5** (0.93 – 2.40 V, MnS re-conversion and CuS re-conversion only with Cu foil as current collector)



**Region 6** (2.40 – 3.00 V, further MnS oxidation)



### 2.3. Electrochemical Performance in Half Cells, In Situ Dilatometry Analysis, and Full Cell Properties

The key electrochemical properties (cycling performance and rate capability) of  $\alpha$ -MnS/SCMFs composite as anode for LIBs are shown in Figure 5. It should be noted that the specific capacity of the  $\alpha$ -MnS/SCMFs-based electrodes is calculated based on the weight of the whole composite, including the SCMFs fraction. Figure 5a displays the galvanostatic (dis)charge tests of  $\alpha$ -MnS/SCMFs and  $\alpha$ -MnS-based electrodes versus lithium metal at a current density of  $50 \text{ mA g}^{-1}$  for the first cycle and of  $200 \text{ mA g}^{-1}$  in the following cycles. Electrodes coated on Cu or Ni foils as current collector are compared. Interestingly, large reversible capacities of 1115 and  $1046 \text{ mAh g}^{-1}$  can be obtained in the first cycle for  $\alpha$ -MnS/SCMFs/Ni and  $\alpha$ -MnS/SCMFs/Cu, respectively. On the other hand, relatively low first coulombic efficiencies (CEs), 67% for  $\alpha$ -MnS/SCMFs/Ni and



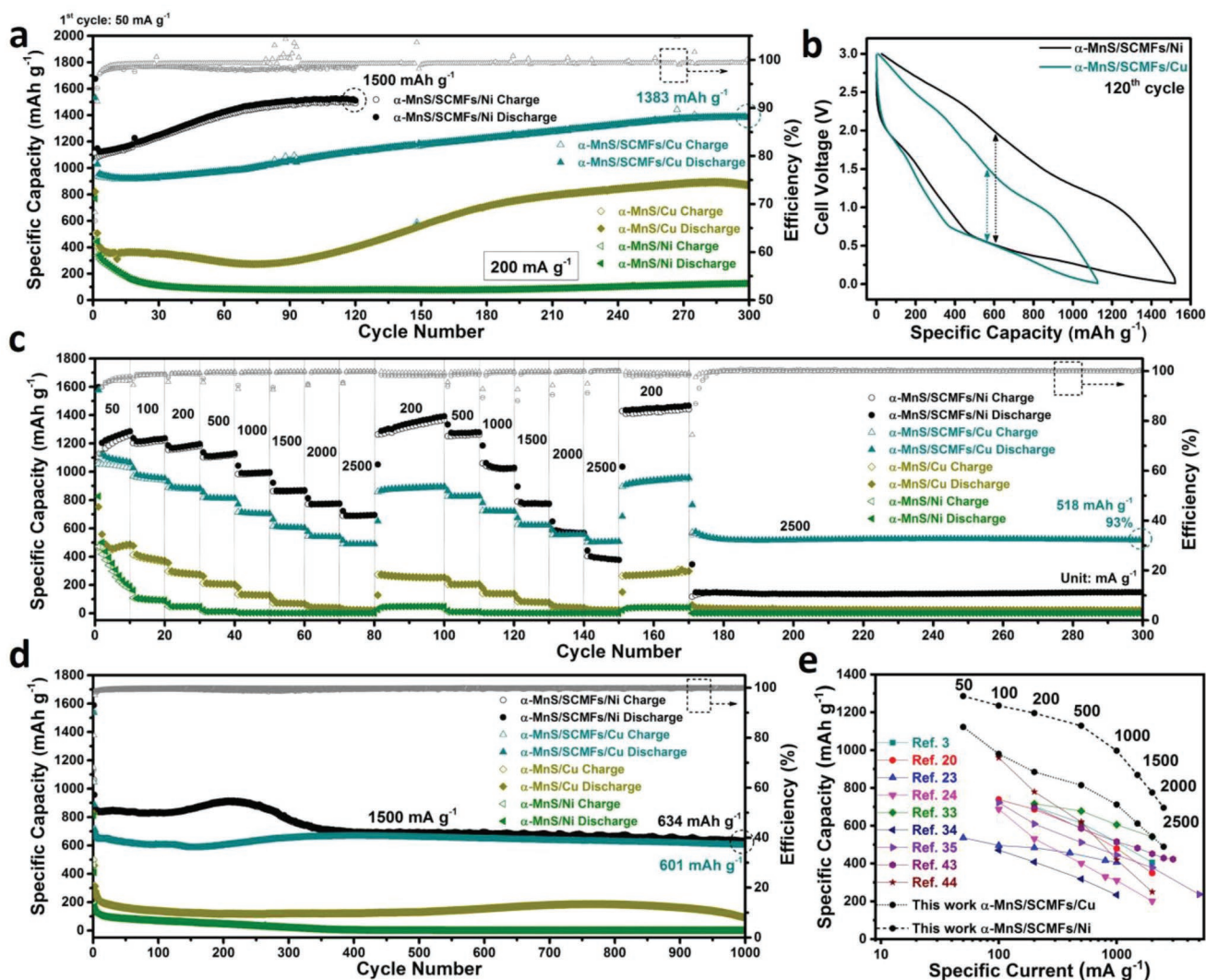


**Figure 5.** Lithium storage performance of  $\alpha$ -MnS/SCMFs and  $\alpha$ -MnS-based electrodes with Cu or Ni foil as current collector in a lithium half-cell configuration. a) (Dis)charge capacity and coulombic efficiency versus cycle number at a constant current density of 50 mA g<sup>-1</sup> for the first cycle and 200 mA g<sup>-1</sup> for the following cycles.  $\Theta$  and  $\Delta$  symbols indicate the coulombic efficiencies of  $\alpha$ -MnS/SCMFs/Ni and  $\alpha$ -MnS/SCMFs/Cu, respectively. b) Corresponding voltage profiles of  $\alpha$ -MnS/SCMFs/Ni (black) and  $\alpha$ -MnS/SCMFs/Cu (cyan) at the 120th cycle. c) Rate capability at various specific currents from 50 to 2500 mA g<sup>-1</sup> for 300 cycles in total. d) “Capacity versus cycle number” at a specific current of 1500 mA g<sup>-1</sup> for 1000 cycles; similarly,  $\Theta$  and  $\Delta$  symbols indicate the coulombic efficiencies of  $\alpha$ -MnS/SCMFs/Ni and  $\alpha$ -MnS/SCMFs/Cu, respectively. e) Comparison of the rate capabilities in this work and in other  $\alpha$ -MnS-based composites reported previously.<sup>[3,20,23,24,33–35,43,44]</sup>

69% for  $\alpha$ -MnS/SCMFs/Cu (a detailed discussion about different first cycle CE for these two electrodes is provided in the Supporting Information (Figure S18, Supporting Information)), are observed mainly resulting from the irreversible SEI formation process. The resulting reversible capacities largely exceed the value obtained for  $\alpha$ -MnS/Ni (446 mAh g<sup>-1</sup>) and  $\alpha$ -MnS/Cu (504 mAh g<sup>-1</sup>), as well as the theoretical capacity of  $\alpha$ -MnS (616 mAh g<sup>-1</sup>). This finding can be explained considering that the nanoscale  $\alpha$ -MnS particles (diameter ranging from 3 to 5 nm) in  $\alpha$ -MnS/SCMFs are likely to provide additional surface storage sites, while the S-doped porous carbon matrix can also offer surface and bulk lithium storage capacity to the  $\alpha$ -MnS/SCMFs-based composite as it has been already proposed in the literature.<sup>[9,39–41]</sup>

Furthermore,  $\alpha$ -MnS/SCMFs/Cu shows a promising long-term performance. During the initial 300 cycles, the reversible capacity gradually increases, finally reaching  $\approx$ 1383 mAh g<sup>-1</sup>. Meanwhile, the CE always remains above 99% between the 10th and 300th cycles, implying that the SEI layer formed on the particle surface is rather stable. The ex situ SEM and TEM images of  $\alpha$ -MnS/SCMFs/Cu collected after 300 cycles (Figure S19, Supporting Information) clearly demonstrate that the original microrod morphology of  $\alpha$ -MnS/SCMFs is maintained upon cycling, supporting our suggestion that the mesoporous carbonaceous framework and the mesoporosity serve as buffer, which can efficiently limit the effect of the active material volume expansion.<sup>[9]</sup> Furthermore, when employing Ni foil as current collector, the corresponding electrode

( $\alpha$ -MnS/SCMFs/Ni) exhibits a higher reversible capacity compared to  $\alpha$ -MnS/SCMFs/Cu (the detailed discussion is reported in the Supporting Information (Figure S20, Supporting Information)). After the first cycle, the capacity of  $\alpha$ -MnS/SCMFs/Ni continuously increases to  $\approx 1500$  mAh  $g^{-1}$  after 120 cycles, although with lower CE compared to  $\alpha$ -MnS/SCMFs/Cu. Such a capacity increase is certainly associated with the “quasi-reversible” SEI formation, a phenomenon that has been reported earlier for several conversion materials.<sup>[4,27,42]</sup> However, as demonstrated by the voltage profile of the 120th cycle (see Figure 5b), the polarization of  $\alpha$ -MnS/SCMFs/Ni is substantially larger than that of  $\alpha$ -MnS/SCMFs/Cu. In fact, unlike  $\alpha$ -MnS/SCMFs/Cu, we found that the layer of the  $\alpha$ -MnS/SCMFs/Ni electrode easily sticks on the separator upon cell disassembly after the prelithiation process. Therefore, the origin of the polarization could be tentatively attributed to the poorer adhesion on the Ni foil, resulting in the exfoliation of the electrode layer, which is also resulting in the low CE of the  $\alpha$ -MnS/SCMFs/Ni electrode from the 10th to the 120th cycle.

According to the kinetic analysis (see above),  $\alpha$ -MnS/SCMFs is a promising material for high power applications. As shown in Figure 5c and Figure S21 (Supporting Information),  $\alpha$ -MnS/SCMFs/Cu exhibits a stable response at all the C rates investigated. For the first C-rate test, specific capacities of 1123, 980, 885, 815, 712, 612, and 543 mAh  $g^{-1}$  are obtained for the applied specific currents of 50, 100, 200, 500, 1000, 1500, and 2000 mA  $g^{-1}$ , respectively. Even at the highest rate of 2500 mA  $g^{-1}$ , a high specific capacity of 489 mAh  $g^{-1}$  is still obtained, indicating that about 50% of the capacity is retained when the applied specific current is increased from 100 to 2500 mA  $g^{-1}$ . More important,  $\alpha$ -MnS/SCMFs/Cu still maintains an outstanding rate capability and cycling stability in the second rate capability test. When the specific current is decreased again 200 mA  $g^{-1}$ , a specific capacity of 909 mAh  $g^{-1}$  is obtained in the 152nd cycle, which increased slightly to 960 mAh  $g^{-1}$  for the 170th cycle, indicating that  $\alpha$ -MnS/SCMFs/Cu possesses excellent reversibility and cycling stability, even after repeated C-rate tests.<sup>[4]</sup> Afterward, we further performed a long-term cycling stability test, using a high specific current of 2500 mA  $g^{-1}$ . The specific capacity is well maintained at a value as high as 518 mAh  $g^{-1}$  in the 300th cycle, accounting for  $\approx 93\%$  capacity retention with respect to the 172nd cycle. Even after 1000 cycles we still obtained 380 mAh  $g^{-1}$  (see Figure S22 of the Supporting Information). In contrast,  $\alpha$ -MnS/Cu shows a substantially lower rate capability (see Figure 5c and Figure S21 of the Supporting Information) with just 211 and 42 mAh  $g^{-1}$  obtained at 500 and 2000 mA  $g^{-1}$  in the first C-rate test. The corresponding results for the second test are 139 and 22 mAh  $g^{-1}$  at 1000 and 2500 mA  $g^{-1}$ , respectively.

Compared to  $\alpha$ -MnS/SCMFs/Cu,  $\alpha$ -MnS/SCMFs/Ni shows higher capacities in the first rate capability test with values of 1286, 1236, 1196, 1129, 997, 869, 776, and 695 mAh  $g^{-1}$  at 50, 100, 200, 500, 1000, 1500, 2000, and 2500 mA  $g^{-1}$ , respectively (see Figure 5c and Figure S21 of the Supporting Information). As the applied rate is lowered again to 200 mA  $g^{-1}$ , a large specific capacity of 1392 mAh  $g^{-1}$  is achieved at the 100th cycle. However, in the second C-rate test and the following long-term cycling an obvious performance decay appears. Comparing the discharge potential profiles of  $\alpha$ -MnS/SCMFs/Cu

and  $\alpha$ -MnS/SCMFs/Ni in the second rate capability test (see Figure S23 of the Supporting Information), we observe a distinctly increasing polarization for  $\alpha$ -MnS/SCMFs/Ni. This may possibly be caused by the already mentioned delamination of the active layer from the current collector, which would also explain the rapid capacity fading of  $\alpha$ -MnS/Ni in the galvanostatic (dis)charge and in the C-rate test. Long-term galvanostatic cycling under the high current density of 1500 mA  $g^{-1}$  was also performed. As shown in Figure 5d,  $\alpha$ -MnS/SCMFs/Cu provides a stable response for 1k cycles, with CE reaching 100% from the tenth cycle on. A specific capacity as high as 601 mAh  $g^{-1}$  is obtained over 1000 cycles, corresponding to 84% capacity retention (with respect to the second cycle capacity). The  $\alpha$ -MnS/SCMFs/Ni electrode still provides 634 mAh  $g^{-1}$  at the 1000th cycle, although showing a distinct capacity fading between the 220th and the 380th cycle. The comparison of the lithium-ion storage performance with previous reports on  $\alpha$ -MnS or  $\alpha$ -MnS-based composites is provided in Figure 5e<sup>[3,20,23,24,33–35,43,44]</sup> and Tables S2 and S3 of the Supporting Information, demonstrating the superior electrochemical performance of  $\alpha$ -MnS/SCMFs in terms of reversible capacity, cycling stability, and rate capability with respect to the large majority of previous works.

To better understand the structural features of  $\alpha$ -MnS/SCMFs-based electrodes, in situ electrochemical dilatometry was employed. Figure 6 displays the electrode thickness variation (cyan line) of  $\alpha$ -MnS/SCMFs/Cu (panel (a)) and  $\alpha$ -MnS/Cu (panel (b)) during the first five galvanostatic (dis)charge cycles (voltage profiles are also shown in black). Obviously, lithiation and delithiation are accompanied by a thickness increase and decrease, respectively. In agreement with the results of the in situ XRD analysis, the relative height change (RHC) curves of  $\alpha$ -MnS/SCMFs/Cu and  $\alpha$ -MnS/Cu in the first discharge can be divided into three regions, i.e., regions 1, 2, and 3. The initially slow thickness change in region 1 can be ascribed to the fact that the capacity in this region mainly stems from (pseudo) capacitive contributions. The charge storage on the surface of the active particles does not result in a serious electrode expansion. The sharp thickness increase, corresponding to the small plateau at around 1.70 V in the discharge profile, is assigned to the conversion reaction of CuS.<sup>[45]</sup> A similarly rapid expansion at 1.70 V is observed in the RHC profile of  $\alpha$ -MnS/Cu (see Figure 6b). In region 2, due to the conversion reaction of  $\alpha$ -MnS and SEI layer formation, the expansion rate of  $\alpha$ -MnS/SCMFs/Cu is distinctly increased. Important, compared with the profile of  $\alpha$ -MnS/SCMFs/Cu, the RHC curve of  $\alpha$ -MnS/Cu shows a steeper slope in region 2, while the thickness of this electrode increased to 29.1%.<sup>[45,46]</sup> Upon further lithiation to 0.01 V, in region 3, the RHC curves of both electrodes show a decreasing expansion rate, since this region only includes charge accumulation and Li-ion insertion into carbon (including the conductive additive).<sup>[45,46]</sup> At the end of the discharge, a total thickness change of 11.3% and 34.1% for  $\alpha$ -MnS/SCMFs/Cu and  $\alpha$ -MnS/Cu is measured, respectively. After the first discharge process, there are two significant points to notice. First, the theoretical size expansion for  $\alpha$ -MnS (60.8%) is much higher than the measured relative changes of the thickness for  $\alpha$ -MnS/SCMFs/Cu (11.3%) and  $\alpha$ -MnS/Cu (34.1%). This can be attributed to the fact that: (i) the electrode contains 20 wt% of conductive

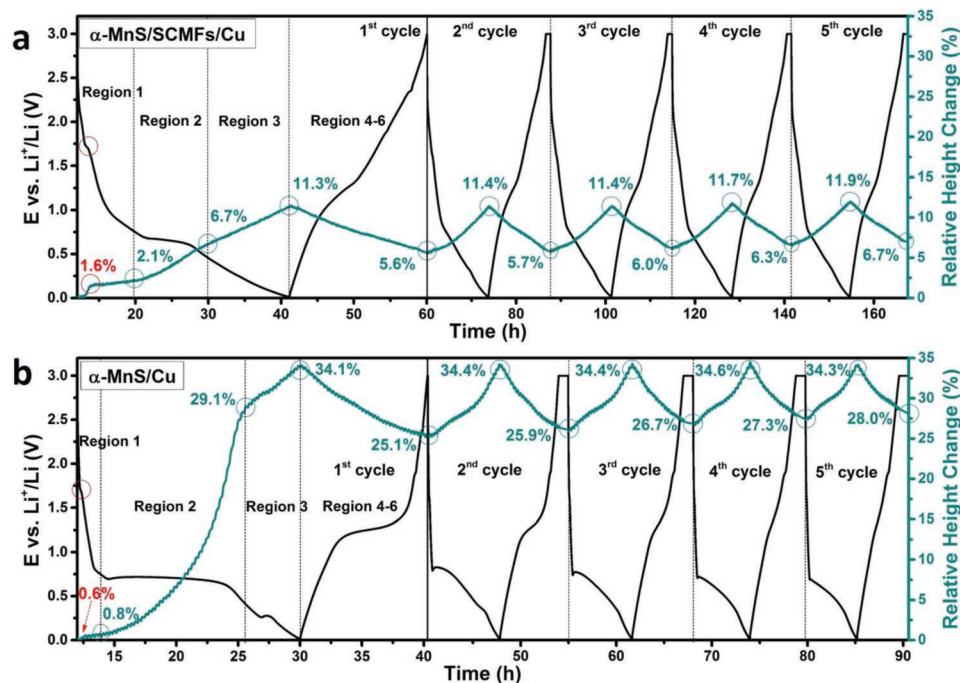


**Figure 6.** In situ dilatometry investigation of  $\alpha$ -MnS/SCMFs/Cu and  $\alpha$ -MnS/Cu: voltage profile and corresponding relative height change of a)  $\alpha$ -MnS/SCMFs/Cu and b)  $\alpha$ -MnS/Cu during the first five cycles. In both cases, the first cycle was performed at  $50 \text{ mA g}^{-1}$  and the following ones were performed at  $70 \text{ mA g}^{-1}$ .

additive and binder, which reduce the volume expansion, and (ii) the electrode network is relatively loose and porous.<sup>[45,47]</sup> Secondly,  $\alpha$ -MnS/SCMFs/Cu shows a smaller expansion in the first cycle compared to  $\alpha$ -MnS/Cu, with the electrode expansion ratio ( $11.3\%/34.1\% = 0.33$ ) being much lower than the active material loading ratio of  $\alpha$ -MnS ( $44\%/80\% = 0.55$ ). This indicates that the mesoporous carbonaceous framework and the graphitic carbon coating have an efficient buffering role, in good agreement with the results of ex situ microscopy studies.<sup>[47,48]</sup> This benefit does not only originate from the carbon content in the  $\alpha$ -MnS/SCMFs-based composite. In fact, the in situ dilatometry investigation of the  $\alpha$ -MnS/SuperC65 with a similar carbon content of  $\alpha$ -MnS/SCMFs (see Figure S24 of the Supporting Information) did not show the same performance, further confirming our conclusion.

Subsequently, upon full charge to 3.0 V, the expansion of  $\alpha$ -MnS/SCMFs/Cu decreases from 11.3% to 5.6%. The origin of the irreversible height change (5.6%) in the first cycle is not yet fully understood. Possibly, it could be attributed to structural electrode reorganization and other irreversible processes such as swelling effect of the electrolyte and SEI formation. Interestingly, Figure 6b shows the irreversible thickness change of  $\alpha$ -MnS/Cu being substantially higher (25.1%). The lower reversible capacity (about  $514 \text{ mAh g}^{-1}$ ; see Figure S26a of the Supporting Information) and coulombic efficiency (57%; see Figure S26a of the Supporting Information) in the first cycle suggest that this irreversible volume expansion of  $\alpha$ -MnS/Cu might be related to incomplete decomposition of  $\text{Li}_2\text{S}$  during delithiation. After the first cycle, the irreversible thickness changes for both electrodes basically decaying to zero upon cycling (see Figure 6 and Figure S26b of the Supporting Information). However,

the thickness change for  $\alpha$ -MnS/Cu is always larger than 7%, meanwhile  $\alpha$ -MnS/Cu just provides a low average specific capacity of  $447 \text{ mAh g}^{-1}$  for the following cycles (second to fifth cycles). Important, the expansion and contraction for  $\alpha$ -MnS/SCMFs/Cu always remain at lower values (around 5%) after the initial cycle while the specific capacity of  $\alpha$ -MnS/SCMFs/Cu is consistently higher than  $900 \text{ mAh g}^{-1}$ . These results, combined with the in situ dilatometry analysis of the  $\alpha$ -MnS/SuperC65-based electrode (Figures S24 and S25, Supporting Information), further confirm the advantageous structural and compositional properties of the  $\alpha$ -MnS/SCMFs composite.

Finally, to evaluate the potential for the practical application of the  $\alpha$ -MnS/SCMFs composite in LIBs, full lithium-ion cells were assembled by coupling  $\alpha$ -MnS/SCMFs/Cu anodes with NCM cathodes as shown in Figure 7a. The NCM-based electrodes exhibit good galvanostatic discharge/charge cycling properties over 100 cycles, with a high specific capacity of 156 and  $137 \text{ mAh g}^{-1}$  at 0.1 C (tenth cycle) and 1.0 C (100th cycle), respectively. However, in order to obtain good performance in the full Li-ion cell, a prelithiation step was necessary for  $\alpha$ -MnS/SCMFs/Cu.<sup>[2,49]</sup> As shown in Figure S27 of the Supporting Information, the  $\alpha$ -MnS/SCMFs/Cu electrode was galvanostatically activated in half-cell configuration for five cycles (final delithiation to 2.0 V), before being assembled in the full Li-ion cell. The  $\alpha$ -MnS/SCMFs/Cu//NCM cell shows excellent performance in the voltage window of 1.0–4.0 V, especially in terms of rate capability (as shown in Figure 7c), with discharge capacities of 153, 149, 142, 136, and  $132 \text{ mAh g}^{-1}$  (with respect to NCM) at 0.1, 0.2, 0.5, 1.0, and 1.5 C, respectively. Even at the highest applied rate of 2.0 C, the full cell could still provide a specific capacity of  $128 \text{ mAh g}^{-1}$ . Importantly, after the C-rate test, the cell shows a



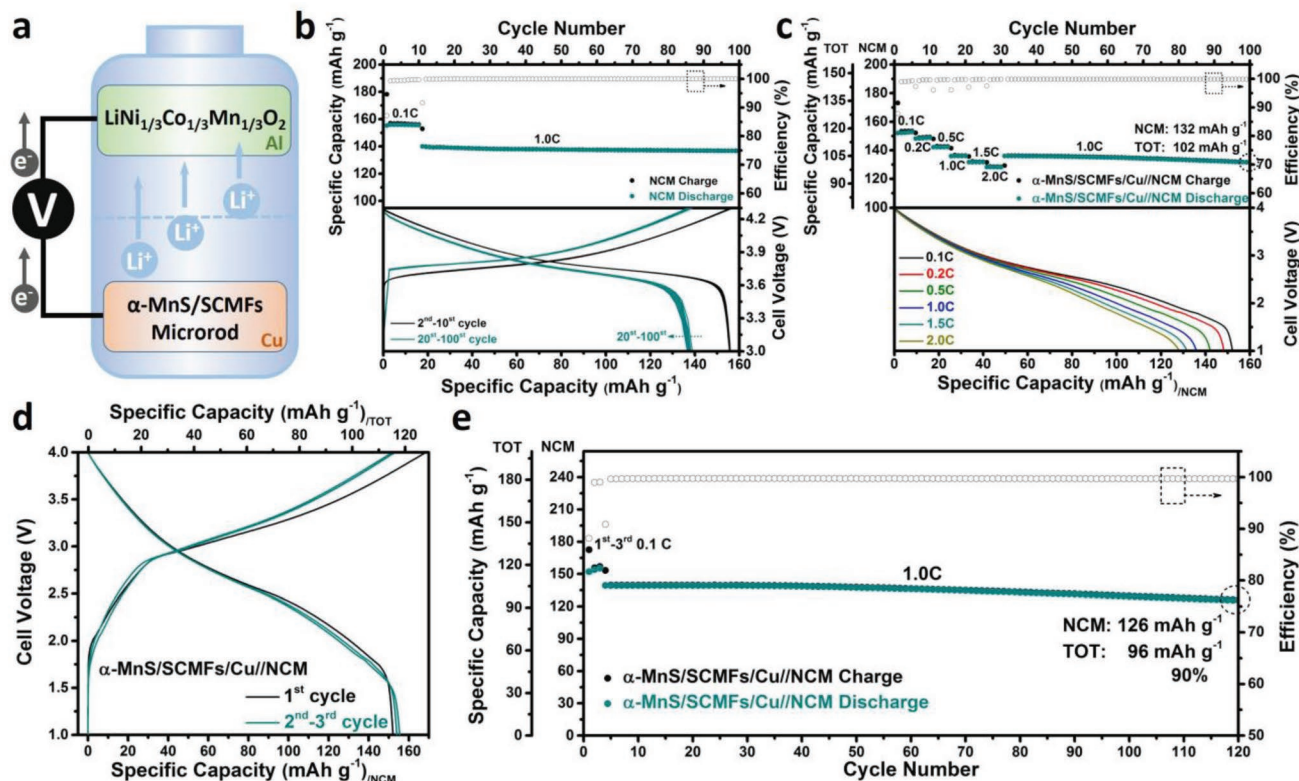


**Figure 7.** Electrochemical performance of  $\alpha$ -MnS/SCMFs/Cu//NCM full Li-ion cells in the voltage range 1.0–4.0 V. a) Schematic presentation of the full cell configuration. b) Charge/discharge-specific capacity and coulombic efficiency during galvanostatic cycling at 0.1 C (first to tenth cycles) and 1.0 C (following 90 cycles) of the NCM-based electrode in a half-cell configuration (upper panel). The corresponding voltage profiles of selected cycles (2nd, 4th, 6th, 8th, 10th, 20th, 30th, 40th, 50th, 60th, 70th, 80th, 90th, and 100th) are shown in the bottom panel. c) Rate capability of the full Li-ion cell at different current rates (from 0.1 to 2.0 C) for 100 cycles in total (upper panel); corresponding discharge profiles for selected cycles (i.e., 3rd, 8th, 13th, 18th, 23rd, and 28th) are shown in the bottom panel. Galvanostatic (dis)charge performance of the full Li-ion cell: d) voltage profiles for the first three cycles at 0.1 C; e) capacity versus cycle number at the constant current rate of 1 C after three initial cycles at 0.1 C. The values of specific capacity for the full cell are referred to the active material amount of the limiting cathode (i.e., NCM) as well as to the sum of cathode and anode masses (i.e., TOT = NCM +  $\alpha$ -MnS/SCMFs); 1.0 C = 161 mA g<sup>-1</sup> (with reference to the cathodic NCM mass).

good cycling stability at 1.0 C, with 132 mAh g<sup>-1</sup> after 100 cycles, which corresponds to 102 mAh g<sup>-1</sup> when considering the active material mass of both electrodes (TOT).<sup>[49]</sup> Figure 7d shows the first three (dis)charge profiles of the full Li-ion cell between 1.0 and 4.0 V at 0.1 C. The cell shows an initial specific discharge capacity of 152 mAh g<sup>-1</sup> (vs NCM) or 116 mAh g<sup>-1</sup> (vs TOT), with a coulombic efficiency of 88%. For the following cycles (second and third cycles), the (dis)charge profile mostly overlaps, suggesting good reversibility. The extended galvanostatic (dis)charge measurements (Figure 7e) demonstrate the excellent cycling stability over 120 cycles with high coulombic efficiency, reaching ≈100% from the fifth cycle on. Also, the  $\alpha$ -MnS/SCMFs/Cu//NCM full cell shows a large reversible capacity of 140 mAh g<sup>-1</sup> (vs NCM) or 106 mAh g<sup>-1</sup> (vs TOT) at 1.0 C (fifth cycle), which is well maintained at 126 mAh g<sup>-1</sup> (vs NCM) or 96 mAh g<sup>-1</sup> (vs TOT) after 120 cycles (Figure 7e), accounting for 90% capacity retention with respect to the fifth cycle.

### 3. Conclusions

In summary, we successfully synthesized a well-defined, microrod composite constituted of  $\alpha$ -MnS nanoparticles finely

embedded in  $\alpha$ -MnS/SCMFs via the simultaneous annealing and sulfidation of a Mn-based MOF. The  $\alpha$ -MnS nanoparticles with sizes in the range of 3–5 nm are well dispersed and uniformly coated by a layered, i.e., graphitic, carbon shell. The resulting  $\alpha$ -MnS/SCMFs composite possesses a number of appealing features, i.e., unique mesoporous structure, S-doped carbon-based frameworks, ultrasmall  $\alpha$ -MnS nanoparticles, strong sulfide-carbon interfacial coupling, and additional electroactive sites.

As a result of the combination of the many beneficial structural and compositional features,  $\alpha$ -MnS/SCMFs shows a lithium storage performance being well superior to that of bulk  $\alpha$ -MnS. Specifically, when Cu foil is used as current collector,  $\alpha$ -MnS/SCMFs/Cu exhibits a large reversible capacity of 1383 mAh g<sup>-1</sup> at the 300th cycle at 0.2 A g<sup>-1</sup> and 601 mAh g<sup>-1</sup> at 1.5 A g<sup>-1</sup> (after 1000 cycles), as well as an outstanding rate capability and high rate cycling properties with 507 mAh g<sup>-1</sup> at 2.5 A g<sup>-1</sup>. Furthermore,  $\alpha$ -MnS/SCMFs/Ni electrodes show an even higher reversible capacity (1500 mAh g<sup>-1</sup> in the 120th cycle) and rate capability (695 mAh g<sup>-1</sup> at 2.5 A g<sup>-1</sup> in the first C-rate test). Interestingly, according to the kinetic analysis, the very fast Li-ion storage in the  $\alpha$ -MnS/SCMFs composite and its

advantageous rate properties mostly originate from a significant (pseudo)capacitive contribution.

Based on the in situ XRD measurements, using different metal foils/disks as current collectors, a new electrochemical reaction mechanism of  $\alpha$ -MnS formation in the first (dis)charge process is proposed, which not only accounts for the dynamic  $\alpha$ -MnS  $\rightarrow$   $\beta$ -MnS phase variation together with  $\text{Li}_2\text{S}$  formation and decomposition during the first cycle, but also explains the partial electrochemical activity of CuS generated during the electrode coating on Cu foil. In situ dilatometry measurements demonstrated the structural advantages of  $\alpha$ -MnS/SCMFs with reduced thickness variation of the electrode during cycling, resulting in the good cycling stability upon repeated (de)lithiation. Highly relevant for applications, also  $\alpha$ -MnS/SCMFs/Cu//NCM full Li-ion cells show a promising rate capability as well as a remarkable cycling stability with a capacity retention of 90% and excellent CE.

The excellent Li-ion storage performance in half/full cell measurements confirms  $\alpha$ -MnS/SCMFs as a highly promising anode material for next-generation LIBs. Importantly, the MOF-driven strategies reported in our work may offer a simple and efficient approach for addressing the low conductivity and volume expansion issues of other TMS-based electrode materials.

## 4. Experimental Section

**Chemicals:** Manganese(II) nitrate tetrahydrate ( $\text{Mn}(\text{NO}_3)_2 \cdot 4\text{H}_2\text{O}$ , > 97%) and sulfur powder (S-powder, 99.98%) were obtained from Sigma-Aldrich Chemical Co. Terephthalic acid (>98%) and manganese(II) sulfide ( $\text{MnS}$ , 99.9%) were purchased from Alfa Aesar Chemical Co. Ethanol (96%) and DMF (99%) were obtained from TechniSolv and EMPLURA, respectively.

**Synthesis of Mn-MOFs:** To synthesize the Mn-MOF precursor,  $\text{Mn}(\text{NO}_3)_2 \cdot 4\text{H}_2\text{O}$  (5 mmol, 1255 mg) and terephthalic acid (5 mmol, 830 mg) were dissolved in 120 mL of mixed solvent (75 mL of DMF and 45 mL of ethanol). The solution was refluxed at 100 °C for 12 h. The obtained white precipitate was collected via centrifugation and washed with ethanol at least five times. Finally, the powder was dried in an oven at 60 °C overnight.

**Synthesis of  $\alpha$ -MnS/SCMFs:** The white Mn-MOF precursor powder was first mixed with sulfur powder (mass ratio of 1:6) in a mortar. The mixture was then heated to 600 °C for 2 h with a heating ramp of 5 °C  $\text{min}^{-1}$  under argon flow in a tube furnace. Subsequently, the furnace was cooled down to room temperature. The resulting product,  $\alpha$ -MnS/SCMFs (black powder), was collected.

**Materials Characterization:** Information about the crystal structure of  $\alpha$ -MnS/SCMFs, Mn-MOF, pure  $\alpha$ -MnS, and other samples was obtained by powder XRD employing a Bruker D8 Advance (Cu-K $\alpha$  radiation with a wavelength of 0.154 nm). Field-emission SEM (ZEISS 1550VP) and TEM (JEOL JEM-3000) measurements were conducted to study the morphology of the Mn-MOFs precursor and pure  $\alpha$ -MnS, and of the  $\alpha$ -MnS/SCMFs microrods. The chemical composition of  $\alpha$ -MnS/SCMFs was determined by element mapping via EDX spectroscopy analysis. Cs-corrected HRTEM was performed to determine the lattice fringes of  $\alpha$ -MnS/SCMFs, using acceleration voltages ranging from 80 to 300 kV (transmission electron microscope FEI Titan 80–300 kV, Eindhoven, the Netherlands). The XPS measurements were carried out with a PHI 5800 MultiTechnique ESCA System using monochromatic Al-K $\alpha$  (1486.6 eV) radiation (250 W, 13 kV), a detection angle of 45°, and pass energies of 93.9 and 29.35 eV for survey and detail spectra, respectively. The main C1s peak was set to 284.8 eV for binding energy calibration. Peak fitting was done with the CasaXPS software using Shirley background

subtraction and mixed Gaussian-Lorentzian peak shapes. A confocal InVia Raman microspectrometer (from Renishaw) with a 633 nm laser was used to analyze  $\alpha$ -MnS/SCMFs. TGA results of  $\alpha$ -MnS/SCMFs and pure  $\alpha$ -MnS were collected with a thermogravimetric analyzer (TA Instruments, Model Q5000), applying a heating ramp of 5 °C  $\text{min}^{-1}$  under air flow. Finally, specific surface area and pore size distribution of  $\alpha$ -MnS/SCMFs were obtained using the  $\text{N}_2$  absorption–desorption isotherms (Autosorb-iQ, Quantachrome) at 77 K, according to the BET and BJH methods, respectively. Each sample was heated at 120 °C for 24 h under vacuum before the measurement.

**Electrodes Preparation:**  $\alpha$ -MnS/SCMFs, pure  $\alpha$ -MnS, and  $\alpha$ -MnS/SuperC65 (pure  $\alpha$ -MnS: 55.1 wt% and SuperC65 (TIMCAL): 44.9 wt%) electrodes were made mixing each active material with conductive carbon (SuperC65) and binder (polyvinylidene fluoride (PVdF)) in the 8:1:1 weight ratio. To prepare the working electrode, first the PVdF powder was dissolved in *N*-methylpyrrolidinone (Sigma-Aldrich) to obtain a 5 wt% solution. Subsequently, the black powders of active material and conductive carbon were dispersed in PVdF-based solution, and then stirred overnight to form the slurry. The resulting slurry was spread onto copper or nickel foil by means of the laboratory doctor blade technique, with a wet film thickness of 120  $\mu\text{m}$ . After the initial drying in an oven at 60 °C (8 h), disk electrodes (12 mm in diameter) were punched and further dried for 24 h at 80 °C under vacuum. The active material mass loading of each disk electrode ( $\alpha$ -MnS/SCMFs, pure  $\alpha$ -MnS or  $\alpha$ -MnS/SuperC65) ranged between 1.0 and 1.1  $\text{mg cm}^{-2}$ . Furthermore, the NCM cathodes used in the full cells consisted of 88 wt% NCM (from Toda) as active material, 7 wt% SuperC65 as carbon additive, and 5 wt% PVdF as binder. The NCM-based slurry was prepared using the same approach as in the anode preparation ( $\alpha$ -MnS/SCMFs), afterward cast on Al foil by means of a laboratory doctor blade (wet film thickness: 60  $\mu\text{m}$ ). The coated electrode was first dried in oven at 60 °C for 6 h and then punched to obtain disk electrodes ( $\phi$  = 12 mm), which were further vacuum dried at 120 °C (6 h). The mass loading of active material (NCM) was about 3.3–3.7  $\text{mg cm}^{-2}$ . For a full cell, in spite of the much larger cathode mass, the substantially lower specific capacity of NCM results in a positive-to-negative capacity ratio of 0.8.

**Electrochemical Measurements:** First, details of the electrochemical performance of  $\alpha$ -MnS/SCMFs,  $\alpha$ -MnS, and NCM-based electrodes were studied in two-electrode 2032 coin cells. The working electrode and lithium metal (counter electrode from Rockwood Lithium, battery grade) were separated by a sheet of glass fiber (GF/D, Whatman) as separator. The electrolyte (from UBE) was 1 mol  $\text{L}^{-1}$   $\text{LiPF}_6$  in ethylene carbonate/diethyl carbonate (EC/DEC, 1:1 by volume) solution with 1% (volume) of vinylene carbonate (VC). For the full cells, the  $\alpha$ -MnS/SCMFs/Cu anode was first preactivated in a half cell (Swagelok-type setup), which was galvanostatically (dis)charged for five cycles and finally charged to 2.0 V in the fifth cycle (see Figure S27 of the Supporting Information). Then, the cell including the preactivated  $\alpha$ -MnS/SCMFs/Cu was disassembled in a glove box (MBraun UNILab) and the electrode washed with fresh electrolyte before being assembled in the full cell. The NCM-based cathode was directly used without any preactivation process. For the electrochemical testing of the full cells, the NCM-based cathode and the preactivated  $\alpha$ -MnS/SCMFs/Cu anode were assembled in coin cells with the same electrolyte (1 m  $\text{LiPF}_6$  in EC/DEC (1/1 volume) with 1% VC). All cells were (dis)assembled in a glove box with  $\text{O}_2$  and  $\text{H}_2\text{O}$  contents below 0.1 ppm. All electrochemical tests were performed at  $20 \pm 2$  °C. CV measurements of the  $\alpha$ -MnS/SCMFs and  $\alpha$ -MnS-based electrodes were conducted within the voltage range from 0.01 to 3.0 V using a VMP3 potentiostat (Biologic Science Instruments). Employing the same instrument, the CV measurements of the current collectors (Cu and Ni foil) were performed after removing the electrode coating layer with the help of a carbon-based adhesive tape.<sup>[50]</sup> The galvanostatic (dis)charge and rate capability measurements were performed with a Maccor 3000 battery tester. The cutoff voltages of anode ( $\alpha$ -MnS/SCMFs and  $\alpha$ -MnS) and cathode (NCM) materials were in the range of 0.01–3.0 V and 3.0–4.3 V, respectively, while the potential window of the full cells ranged from 1.0 to 4.0 V.

**In Situ XRD Analysis:** In situ XRD measurements with  $\alpha$ -MnS/SCMFs upon galvanostatic lithiation and delithiation were carried out in a specific self-designed two-electrode cell.<sup>[4,9,32]</sup> For the working electrode preparation, a  $\alpha$ -MnS/SCMFs-based slurry similar to the one described above (preparation of working electrodes), which was composed of 70 wt%  $\alpha$ -MnS/SCMFs, 15 wt% SuperC65, and 15 wt% PVdF, was cast on a Be disk, serving as current collector and “window” for the X-ray beams at the same time (wet thickness of 250  $\mu$ m). The resulting working electrode was first dried in an oven at 60 °C for 1–2 h and then vacuum dried at 50 °C overnight. In the in situ cell, the working electrode and lithium metal counter electrode were separated by a bilayer of Whatman glass fiber, which was drenched with 350  $\mu$ L of 1 M LiPF<sub>6</sub> in EC/DEC (1:1 vol) with 1% VC. Each XRD pattern was recorded over a time span of  $\approx$ 45 min including 60 s rest time for each pattern). Simultaneously, the galvanostatic first discharge/charge experiment of the in situ cell was performed via a potentiostat/galvanostat (SP-150, BioLogic) with a specific current of 50 mA g<sup>-1</sup>, in the voltage range of 0.01–3.0 V.

**In Situ Dilatometry Analysis:** In situ electrochemical dilatometry measurements of  $\alpha$ -MnS/SCMFs/Cu,  $\alpha$ -MnS/Cu, and  $\alpha$ -MnS/SuperC65/Cu were performed using an ECD-3 Nano Dilatometer cell (from EL-CELL GmbH). In the in situ dilatometry cell, the diameter of the working electrode was 10 mm with thicknesses of 45  $\mu$ m for  $\alpha$ -MnS/SCMFs/Cu, 38  $\mu$ m for  $\alpha$ -MnS/Cu, and 43  $\mu$ m for  $\alpha$ -MnS/SuperC65/Cu. Lithium metal foils served as counter electrode and reference, and a specific glass T-frit as separator, which was soaked with the same electrolyte as mentioned above. During each measurement, the dilatometer cell was held in a climatic chamber (Binder KB 23, Germany) to keep a stationary temperature of 20 °C. Prior to each measurement, the assembled dilatometry cells were allowed to rest (OCV) for 12 h. Galvanostatic (de)lithiation experiments were carried out using an SP-150 potentiostat (from Bio-logic Science Instruments) with a single channel, applying a specific current of 50 mA g<sup>-1</sup> in the first cycle and 70 mA g<sup>-1</sup> in the second to fifth cycles. The thickness variation of the working electrode was recorded by using an E-852 controller box (PISeca Signal Conditioner) and the EC-Lab software.

## Supporting Information

Supporting Information is available from the Wiley Online Library or from the author.

## Acknowledgements

The authors thank Huang Zhang for valuable discussions. Y.M. and Y.-J.M. gratefully acknowledge financial support from the China Scholarship Council (CSC; Grant Nos. 201608080085 and 201608080094). Financial support from the Helmholtz Association, Karlsruhe Institute of Technology, and Ulm University is also acknowledged. Moreover, the authors would like to thank Yuanchun Ji for TEM measurements. This work contributes to the research performed at CELEST (Center for Electrochemical Energy Storage Ulm-Karlsruhe).

## Conflict of Interest

The authors declare no conflict of interest.

## Keywords

$\alpha$ -MnS nanoparticles, in situ dilatometry, in situ XRD/reaction mechanism, lithium-ion batteries, S-doped carbonaceous frameworks

Received: June 27, 2019

Revised: July 18, 2019

Published online: October 1, 2019

- [1] D. Bresser, S. Passerini, B. Scrosati, *Energy Environ. Sci.* **2016**, *9*, 3348.
- [2] S. Chen, L. Shen, P. A. van Aken, J. Maier, Y. Yu, *Adv. Mater.* **2017**, *29*, 1605650.
- [3] X. Gao, B. Wang, Y. Zhang, H. Liu, H. Liu, H. Wu, S. Dou, *Energy Storage Mater.* **2019**, *16*, 46.
- [4] Y. Ma, Y. Ma, D. Bresser, Y. Ji, D. Geiger, U. Kaiser, C. Streb, A. Varzi, S. Passerini, *ACS Nano* **2018**, *12*, 7220.
- [5] P. Lou, Z. Cui, Z. Jia, J. Sun, Y. Tan, X. Guo, *ACS Nano* **2017**, *11*, 3705.
- [6] Y. Ma, U. Ulissi, D. Bresser, Y. Ma, Y. Ji, S. Passerini, *Electrochim. Acta* **2017**, *258*, 535.
- [7] D.-H. Liu, W.-H. Li, Y.-P. Zheng, Z. Cui, X. Yan, D.-S. Liu, J. Wang, Y. Zhang, H.-Y. Lü, F.-Y. Bai, J.-Z. Guo, X.-L. Wu, *Adv. Mater.* **2018**, *30*, 1706317.
- [8] Q. Wang, R. Zou, W. Xia, J. Ma, B. Qiu, A. Mahmood, R. Zhao, Y. Yang, D. Xia, Q. Xu, *Small* **2015**, *11*, 2511.
- [9] Y. Ma, Y. Ma, D. Geiger, U. Kaiser, H. Zhang, G.-T. Kim, T. Diemant, R. J. Behm, A. Varzi, S. Passerini, *Nano Energy* **2017**, *42*, 341.
- [10] Z.-S. Wu, W. Ren, L. Xu, F. Li, H.-M. Cheng, *ACS Nano* **2011**, *5*, 5463.
- [11] R. Wu, D. P. Wang, X. Rui, B. Liu, K. Zhou, A. W. K. Law, Q. Yan, J. Wei, Z. Chen, *Adv. Mater.* **2015**, *27*, 3038.
- [12] Y. Hao, C. Chen, X. Yang, G. Xiao, B. Zou, J. Yang, C. Wang, *J. Power Sources* **2017**, *338*, 9.
- [13] H. Furukawa, K. E. Cordova, M. O’Keeffe, O. M. Yaghi, *Science* **2013**, *341*, 1230444.
- [14] W. Xia, A. Mahmood, R. Zou, Q. Xu, *Energy Environ. Sci.* **2015**, *8*, 1837.
- [15] Y. Ma, H. Ma, Z. Yang, J. Ma, Y. Su, W. Li, Z. Lei, *Langmuir* **2015**, *31*, 4916.
- [16] S. J. Yang, S. Nam, T. Kim, J. H. Im, H. Jung, J. H. Kang, S. Wi, B. Park, C. R. Park, *J. Am. Chem. Soc.* **2013**, *135*, 7394.
- [17] W. Huang, S. Li, X. Cao, C. Hou, Z. Zhang, J. Feng, L. Ci, P. Si, Q. Chi, *ACS Sustainable Chem. Eng.* **2017**, *5*, 5039.
- [18] J. H. Lee, Y. J. Sa, T. K. Kim, H. R. Moon, S. H. Joo, *J. Mater. Chem. A* **2014**, *2*, 10435.
- [19] M. Oku, K. Hirokawa, S. Ikeda, *J. Electron Spectrosc. Relat. Phenom.* **1975**, *7*, 465.
- [20] B. Liu, Z. Liu, D. Li, P. Guo, D. Liu, X. Shang, M. Lv, D. He, *Appl. Surf. Sci.* **2017**, *416*, 858.
- [21] D. Sun, Y. Tang, D. Ye, J. Yan, H. Zhou, H. Wang, *ACS Appl. Mater. Interfaces* **2017**, *9*, 5254.
- [22] F. Zheng, Z. Yin, H. Xia, G. Bai, Y. Zhang, *Chem. Eng. J.* **2017**, *327*, 474.
- [23] Y. Liu, Y. Qiao, W.-X. Zhang, Z. Li, X.-L. Hu, L.-X. Yuan, Y.-H. Huang, *J. Mater. Chem.* **2012**, *22*, 24026.
- [24] D. Wang, D. Cai, B. Qu, T. Wang, *CrystEngComm* **2016**, *18*, 6200.
- [25] G. Li, B. He, M. Zhou, G. Wang, N. Zhou, W. Xu, Z. Hou, *ChemElectroChem* **2017**, *4*, 81.
- [26] G. A. Muller, J. B. Cook, H.-S. Kim, S. H. Tolbert, B. Dunn, *Nano Lett.* **2015**, *15*, 1911.
- [27] D. Bresser, E. Paillard, R. Kloepsch, S. Krueger, M. Fiedler, R. Schmitz, D. Baither, M. Winter, S. Passerini, *Adv. Energy Mater.* **2013**, *3*, 513.
- [28] V. Augustyn, J. Come, M. A. Lowe, J. W. Kim, P.-L. Taberna, S. H. Tolbert, H. D. Abruña, P. Simon, B. Dunn, *Nat. Mater.* **2013**, *12*, 518.
- [29] D. Chao, P. Liang, Z. Chen, L. Bai, H. Shen, X. Liu, X. Xia, Y. Zhao, S. V. Savilov, J. Lin, Z. X. Shen, *ACS Nano* **2016**, *10*, 10211.
- [30] R. Wang, B. Li, L. Lai, M. Hou, J. Gao, R. Wu, *Chem. Eng. J.* **2019**, *355*, 752.
- [31] Y. Liu, L. Li, J. Zhu, T. Meng, L. Ma, H. Zhang, M. Xu, J. Jiang, C. M. Li, *ACS Appl. Mater. Interfaces* **2018**, *10*, 27911.



- [32] Y. Ma, Y. Ma, G. Giuli, T. Diemant, R. J. Behm, D. Geiger, U. Kaiser, U. Ulissi, S. Passerini, D. Bresser, *Sustainable Energy Fuels* **2018**, *2*, 2601.
- [33] C. Wu, J. Maier, Y. Yu, *Adv. Mater.* **2016**, *28*, 174.
- [34] J. Ning, D. Zhang, H. Song, X. Chen, J. Zhou, *J. Mater. Chem. A* **2016**, *4*, 12098.
- [35] S. Gao, G. Chen, Y. Dall'Agnese, Y. Wei, Z. Gao, Y. Gao, *Chem. - Eur. J.* **2018**, *24*, 13535.
- [36] D. Yuan, G. Huang, F. Zhang, D. Yin, L. Wang, *Electrochim. Acta* **2016**, *203*, 238.
- [37] D. Aurbach, Y. Ein-Eli, *J. Electrochem. Soc.* **1995**, *142*, 1746.
- [38] K. Cao, L. Jiao, H. Xu, H. Liu, H. Kang, Y. Zhao, Y. Liu, Y. Wang, H. Yuan, *Adv. Sci.* **2016**, *3*, 1500185.
- [39] D. Bresser, E. Paillard, P. Niehoff, S. Krueger, F. Mueller, M. Winter, S. Passerini, *ChemPhysChem* **2014**, *15*, 2177.
- [40] B. Liu, Q. Zhang, Z. Jin, L. Zhang, L. Li, Z. Gao, C. Wang, H. Xie, Z. Su, *Adv. Energy Mater.* **2018**, *8*, 1702347.
- [41] F. Zheng, M. He, Y. Yang, Q. Chen, *Nanoscale* **2015**, *7*, 3410.
- [42] A. Ponrouch, P.-L. Taberna, P. Simon, M. R. Palacín, *Electrochim. Acta* **2012**, *61*, 13.
- [43] K. M. Jeon, J. S. Cho, Y. C. Kang, *J. Power Sources* **2015**, 295, 9.
- [44] D. Chen, H. Quan, X. Luo, S. Luo, *Scr. Mater.* **2014**, 76, 1.
- [45] Y. Zhao, L. P. Wang, M. T. Sougrati, Z. Feng, Y. Leconte, A. Fisher, M. Srinivasan, Z. Xu, *Adv. Energy Mater.* **2017**, *7*, 1601424.
- [46] M. R. Palacín, *Chem. Soc. Rev.* **2009**, *38*, 2565.
- [47] J. Kim, M. K. Chung, B. H. Ka, J. H. Ku, S. Park, J. Ryu, S. M. Oh, *J. Electrochem. Soc.* **2010**, *157*, A412.
- [48] H.-K. Kim, K. C. Roh, K.-B. Kim, *J. Electrochem. Soc.* **2015**, *162*, A2308.
- [49] A. Varzi, D. Bresser, J. von Zamory, F. Müller, S. Passerini, *Adv. Energy Mater.* **2014**, *4*, 1400054.
- [50] M. Kuenzel, D. Bresser, T. Diemant, D. V. Carvalho, G.-T. Kim, R. J. Behm, S. Passerini, *ChemSusChem* **2018**, *11*, 562.